

COMPARING THE LIGHT CURVES OF SIMULATED TYPE IA SUPERNOVAE WITH OBSERVATIONS USING DATA-DRIVEN MODELS

BENEDIKT DIEMER^{1,2,3}, RICHARD KESSLER^{2,3,1}, CARLO GRAZIANI^{1,2}, GEORGE C. JORDAN IV^{1,2}, DONALD Q. LAMB^{1,2,4}, MIN LONG^{1,2}, AND DANIEL R. VAN ROSSUM^{1,2}

¹ Flash Center for Computational Science, The University of Chicago, Chicago, IL 60637, USA; bdiemer@oddjob.uchicago.edu

² Department of Astronomy & Astrophysics, The University of Chicago, Chicago, IL 60637 USA

³ Kavli Institute for Cosmological Physics, The University of Chicago, Chicago, IL 60637 USA

⁴ Enrico Fermi Institute, The University of Chicago, Chicago, IL 60637 USA

Received 2012 March 5; accepted 2013 June 21; published 2013 August 1

ABSTRACT

We propose a robust, quantitative method to compare the synthetic light curves of a Type Ia supernova (SNIa) explosion model with a large set of observed SNeIa, and derive a figure of merit for the explosion model's agreement with observations. The synthetic light curves are fit with the data-driven model SALT2 which returns values for stretch, color, and magnitude at peak brightness, as well as a goodness-of-fit parameter. Each fit is performed multiple times with different choices of filter bands and epoch range in order to quantify the systematic uncertainty on the fitted parameters. We use a parametric population model for the distribution of observed SNIa parameters from large surveys, and extend it to represent red, dim, and bright outliers found in a low-redshift SNIa data set. We discuss the potential uncertainties of this population model and find it to be reliable given the current uncertainties on cosmological parameters. Using our population model, we assign each set of fitted parameters a likelihood of being observed in nature, and a figure of merit based on this likelihood. We define a second figure of merit based on the quality of the light curve fit, and combine the two measures into an overall figure of merit for each explosion model. We compute figures of merit for a variety of one-, two-, and three-dimensional explosion models and show that our evaluation method allows meaningful inferences across a wide range of light curve quality and fitted parameters.

Keywords: supernovae: general

1. INTRODUCTION

Due to their value as cosmological distance indicators (Riess et al. 1998; Perlmutter et al. 1999), Type Ia supernovae (hereafter SNeIa) have received intense observational attention, with large-scale SN surveys exponentially increasing the number of observed SNIa events (see, e.g., Goobar & Leibundgut 2011, for a review). This trend will continue over the next decade with even larger data sets from the Dark Energy Survey (DES, Bernstein et al. 2012), Pan-STARRS (Tonry et al. 2012) and the Large Synoptic Survey Telescope (Ivezic et al. 2008). These surveys also undertake strong efforts to overcome calibration issues, which currently represent the largest source of uncertainty in using SNeIa to measure of the dark energy equation of state parameter w (Conley et al. 2011). As calibration uncertainties are reduced, astrophysical uncertainties become a larger fraction of the total error budget, and a theoretical understanding of SNeIa may help to reduce those uncertainties. For example, after a decade of observational efforts to reduce the intrinsic Hubble scatter, only modest progress has been made (see, e.g., Silverman et al. 2012, for a thorough analysis). Thus, we will need better theoretical models of SNeIa to understand the nature of intrinsic scatter, and other systematics such as the correlation with host galaxy environment (Kelly et al. 2010; Lampeitl et al. 2010; Sullivan et al. 2011). A theoretical framework might lead to a physically motivated parameterization of these effects with measurable parameters.

Unfortunately, current theoretical models are not yet able to investigate subtle systematic effects like these. While the general consensus is that SNeIa arise from the thermonuclear explosion of a white dwarf in a binary system (Whelan & Iben 1973), it is still unclear whether the companion star is a

main sequence star or red giant (single-degenerate scenario), or another white dwarf (double-degenerate scenario, Iben & Tutukov 1984). Recent observations disfavor the red giant scenario (Li et al. 2011a; Brown et al. 2012), but the question is far from settled (see, e.g., Maoz & Mannucci 2012, for a review). Even within the single-degenerate paradigm there is still no consensus as to the exact explosion mechanism (see, e.g., Hillebrandt & Niemeyer 2000, for a review). The deflagration-to-detonation model (DDT, or delayed detonation, DD, e.g. Khokhlov 1991; Niemeyer & Hillebrandt 1995; Niemeyer 1999; Kasen et al. 2009; Krueger et al. 2012; Seitzzahl et al. 2013) has emerged as the most popular model, but the exact mechanism by which a detonation is initiated is still unknown (Röpke 2007; Woosley 2007; Woosley et al. 2009). Furthermore, the field has only recently moved on to three-dimensional (3D) simulations, and results suggest that, due to the effects of turbulence, lower-dimensional results are not reliable (Röpke & Niemeyer 2007). Another surprising result of multi-dimensional simulations was the discovery of an alternative explosion mechanism, the gravitationally confined detonation (GCD; Plewa et al. 2004; Townsley et al. 2007; Jordan et al. 2008; Meakin et al. 2009; Jordan et al. 2012b). Besides the DDT and GCD, a variety of other models has been investigated, such as the double-degenerate scenario (Dan et al. 2011, 2012; Pakmor et al. 2012), double-detonation and sub-Chandrasekhar models (Livne & Arnett 1995; Shen et al. 2010; Kromer et al. 2010), and failed detonation models (Jordan et al. 2012a; Kromer et al. 2013).

With such a multitude of possible explosion models at hand, we need to use observed SNeIa to discern between promising and invalid models. The main difficulty in performing such validation is that SNIa light curves and spectra are quite di-

verse, meaning that there is no master light curve or spectral template to compare against explosion models (Höflich et al. 1996; Nugent et al. 2002; Benetti et al. 2005; Branch et al. 2006; Hayden et al. 2010; Blondin et al. 2012). Generally, two methods of comparing theoretical models and observations have been employed: visual comparisons of light curves and spectra, and comparisons of characteristic magnitudes, colors and decline rates. Visual comparisons entail overplotting spectra or light curves of the explosion model in question and one or a few observed events. The obvious advantage is simplicity, but (1) one or a few observed events are not representative of SNeIa as a whole, (2) the results of visual comparisons are subjective, and (3) the human eye easily misses details, especially when plotting on a logarithmic scale. An alternative method is to reduce the high-dimensional space of light curves to a few characteristic quantities such as peak magnitude, Δm_{15} (Phillips 1993) and $B - V$ color. For example, Khokhlov et al. (1993) and Livne & Arnett (1995) used the peak magnitudes and rise times of their explosion model light curves to compare to observed data, and find these quantities to discern between favored and disfavored models. Over time, modelers extended such comparisons to quantities describing the decline rate, such as $\Delta m_{V,20}$ or Δm_{15} (see, e.g., Höflich et al. 1996; Höflich & Khokhlov 1996) and used multi-color light curves as well as spectra (see, e.g., Kasen & Plewa 2007; Blondin et al. 2011, 2013). Höflich et al. (2010) devised a method to directly infer physical parameters such as the metallicity and central density of the progenitor by comparing their impact on the light curves with observations. Despite all these efforts, robust methods to evaluate models remain elusive. Röpke et al. (2012) attempted to discern between a double-degenerate model from Pakmor et al. (2012) and a DDT model using the recently observed SN 2011fe (Nugent et al. 2011). Despite the very different explosion mechanisms, they concluded it was difficult to verify or falsify either model.

The main weakness of many of the aforementioned comparison methods is that they employ only a small subset of the available data, either particular SNeIa which may or may not be representative of the overall sample, or quantities such as peak magnitudes and Δm_{15} which rely on one or a few measurements in a particular filter band. Besides the somewhat arbitrary definition of those quantities, much attention is often given to the width-luminosity relation (Phillips relation, Phillips 1993; Phillips et al. 1999; Kasen & Woosley 2007), though the color-magnitude relation is equally important for standardizing peak magnitudes, and hence for cosmology (Riess et al. 1996b; Tripp 1998; Wang et al. 2003). Nevertheless, the comparison methods described above were appropriate when only a few SNeIa had been observed with good accuracy. With modern data sets in hand, however, we are now in a position to compare theoretical models with a well-understood set of observed SNeIa. The observational community uses data-driven models such as SALT2 (Guy et al. 2007), SiFTO (Conley et al. 2008), mlcs2k2 (Jha et al. 2007) and SNooPy (Burns et al. 2011) to fit observed light curves and extract a few meaningful parameters which summarize the properties of the light curves in question. The results of those fits, such as stretch, color and magnitude, are used to derive distance moduli for a Hubble diagram. We thus expect that these fitting techniques should also work well for comparing theoretical light curves to observations.

Blondin et al. (2011) applied data-driven models to the synthetic light curves of Kasen et al. (2009), but concluded that

neither mlcs2k2, SALT2 nor SNooPy fit the light curves to sufficient accuracy, and thus focus on rise and decline times, color evolution and spectral comparisons. In this paper, we propose a somewhat different approach. We define a quantitative measure of light curve quality for all explosion models, including those that are not well fit by data-driven models. Though we appreciate the value of spectral comparisons, we focus on broadband quantities. By virtue of averaging over the range of wavelengths in a filter band, the light curves of explosion models are less sensitive to the details of the radiative transport treatment than the spectral features. Secondly, the properties of observed light curves have already been captured in data-driven models which allow us to infer characteristic quantities for a given explosion model. Spectral comparison codes such as SNID (Blondin & Tonry 2011) quantify how well a spectrum matches a set of templates, but do not result in any summarizing quantities such as color and stretch.

Our goal is to design a comparison method which satisfies three main criteria, namely (1) avoids arbitrarily picking a sub-set of the data such as particular SNeIa, (2) uses quantities which reflect the entire light curve rather than a few particular data points such as the epoch of peak brightness, and (3) results in a well-defined figure of merit, allowing us to rank explosion models by how well they reproduce observations. Our strategy is to fit the explosion model light curves with SALT2 and compare the fitted stretch, color and peak magnitude to the measured population of normal SNeIa, ignoring peculiar events.¹ This procedure returns two separate indicators of light curve quality, namely how well the light curves in question can be fit with SALT2, and how likely the fitted stretch, color and peak magnitude are to be observed in nature. These two indicators are combined into an overall figure of merit. We emphasize that this figure of merit should be seen as a relative measure of comparison between a set of explosion models rather than an absolute measure of quality, chiefly because any changes in the SALT2 model or its uncertainties (e.g. through re-training), or any changes in the exact fitting procedure, will lead to different results.

The details of our method are described in Section 2. In Section 3, we give the results of applying our fitting procedure to a range of explosion models. We discuss potential shortcomings of our method in Section 4, and summarize our results in Section 5.

2. METHOD

The goal of our analysis is to derive a figure of merit indicating how likely it is that a given explosion model represents observed SNeIa. Figure 1 gives an overview of the different stages of this procedure. In Section 2.1 we discuss the hydrodynamic simulations and radiative transfer codes used in this analysis, as well as the conversion from spectral energy distributions (SEDs) to light curves. In Section 2.2 we introduce data-driven models, and summarize the most important features of the SALT2 model. In Section 2.3 we describe our method for fitting explosion model light curves with the SALT2 model, and discuss how we derive a goodness-of-fit indicator as well as fitted parameters. In Section 2.4 we describe the population model of SNeIa in stretch-color-magnitude space. In Section 2.5 we define figures of merit

¹ Peculiar SNeIa include events such as 2002cx (Wood-Vasey et al. 2002; Li et al. 2003), 2005gj (Aldering et al. 2006; Prieto et al. 2007) and 2005hk (Chornock et al. 2006; Phillips et al. 2007). See also Foley et al. (2013) and references therein.

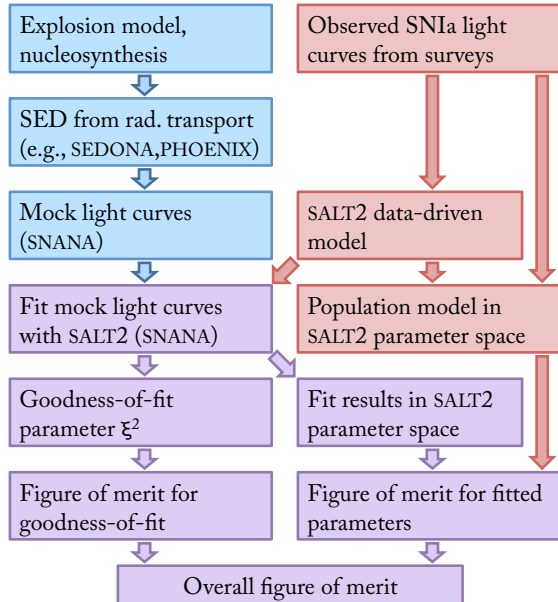


Figure 1. Flow chart representation of our procedure for comparing explosion models to observed SNeIa. Blue boxes represent purely modeling-related steps, i.e., stages in the process where no comparison with observations has taken place yet. Conversely, red boxes mark purely observational stages. Purple boxes represent stages where information from both simulations and observations has been combined.

for goodness-of-fit and fitted parameters, and combine them into an overall figure of merit.

2.1. Explosion Models and Radiative Transfer

We are not aiming to introduce new explosion models, or to discuss the details of hydrodynamic simulations, but to use light curves of various explosion models to test our evaluation method. For this purpose, we pick four classes of models which we expect to provide interesting test cases for our method. Namely, we use the well-studied W7 model, the delayed-detonation models of Kasen et al. (2009, hereafter KRW09), a recent suite of pure deflagration models (M. Long et al. 2013, in preparation), as well as a suite of phenomenological, pre-expanded models. These models represent very different classes of explosions, and were computed in one dimension (1D, W7), two dimensions (2D, KRW09, pre-expanded) and 3D (pure deflagration; light curves for the pure deflagration models were computed in 1D). We briefly discuss these models below.

The W7 model (Nomoto et al. 1984; Thielemann et al. 1986) is a 1D parameterized explosion model. The white dwarf does not detonate, but produces a bright explosion due to a fast deflagration. Despite its simplicity, many radiation transport studies have found W7 to reproduce observed light curves and spectra surprisingly well (Jeffery et al. 1992; Höflich 1995; Nugent et al. 1997; Baron et al. 2006; Kasen et al. 2006; Kromer & Sim 2009; van Rossum 2012).

The KRW09 models are discussed in detail in the original paper, as well as in Blondin et al. (2011). The suite consists of 43 2D delayed-detonation (otherwise known as DDT) explosion models. All models are based on the same progenitor model, but have different distributions of the initial flame bubbles, as well as different detonation criteria. The isotropic (iso) models, as well as one asymmetric model (asym_1), were given an isotropic distribution of between 20 and 150

flame bubbles. For the other asymmetric models, between 15 and 105 flame bubbles were distributed within a cone of a certain solid angle. The second distinguishing feature is the detonation criterion (dc), where each detonation criterion corresponds to a certain range of densities, as well as a minimum Karlovitz number which has often been used as a criterion for detonation (see, e.g., Niemeyer & Woosley 1997). More details on the model setups are given in the supplement to KRW09. The spectral and light curve comparisons in Blondin et al. (2011) showed that some of the KRW09 models agree well with observations, while others are incompatible with observed spectra.

Pure deflagration models rely on the initial deflagration to consume and unbind the white dwarf. Thus, they tend to burn less material to ^{56}Ni than detonating models, and produce events which are dimmer than standard SNeIa. We use the light curves of a recently completed suite of six pure deflagration models (M. Long et al. 2013, in preparation). These high-resolution, 3D simulations were computed using the FLASH code (Fryxell et al. 2000) and follow the deflagration of a $1.365 M_{\odot}$ white dwarf. The white dwarf was ignited with a certain number of ignition bubbles, distributed in a sphere centered at the origin. The models are labeled by the number of ignition bubbles (between 63 and 3500) as well as the radius of the sphere (128–384 km), e.g., “PureDef_0063_128”. The explosions produce between 0.13 and $0.29 M_{\odot}$ of ^{56}Ni .

Finally, we use three 2D, phenomenological, off-centered detonation models. These models were created by expanding an initially stable, Chandrasekhar-mass, white dwarf with a radial velocity. The total expansion energy was equivalent to 30%, 60% and 80% of the binding energy, respectively. We allow the white dwarf to expand, reach its maximum expansion and contract. We trigger a detonation during the contracting phase of the WD by artificially creating a high-temperature region offset from the WD’s center. This scenario is designed to investigate strong asphericity, and thus strong variations of light curves with viewing angle. The simulations were computed with the FLASH code. In the rest of the paper, we refer to these models as “pre-expanded” models.

SEDs for each explosion model were computed using two different radiative transfer codes, Sedona (KRW09 and pre-expanded models) and Phoenix (W7 and pure deflagration models).

Sedona (Kasen et al. 2006) is a Monte-Carlo code which sends a large number of photon packets through the ejecta, and eventually bins them into an SED. The version of Sedona used can handle 2D, and thus returns spectra as a function of viewing angle. Due to the nature of the Monte-Carlo method, the code returns Poisson uncertainties on the SEDs due to the finite number of photon packages used. However, when integrating the SEDs to obtain light curves, the number of photon packets in each broadband filter is generally so large that the Poisson error is negligible. For all models with Sedona radiative transport, 30 viewing angles were computed. The cosine of the viewing angles were evenly spaced, so that each viewing angle has equal chance of being observed. The viewing angles quoted refer to the mean cosine of the segment in solid angle, ranging from 15° (the south pole) to 165° (the north pole).

The second radiation transport code used was Phoenix (Hauschildt & Baron 1999, 2004; van Rossum 2012). Phoenix numerically solves the special relativistic radiative transfer equation using the efficient and highly accurate short

characteristic and operator splitting methods. It samples millions of atomic lines individually, and solves for the two-way interaction between the radiation field and matter in a self-consistent manner (i.e., avoiding the use of the local thermodynamic equilibrium approximation, and thus free scattering parameters). Phoenix solves for the time evolution using the radiation energy balance method. The code does not use the Sobolev approximation, diffusion approximations or opacity binning. Phoenix operates in 1D, assuming spherical symmetry.

The SEDs from Sedona start 2.5 days after explosion, with a cadence of one day, and in wavelength bins of 10 Å. The Phoenix SEDs for W7 start 4 days after explosion, with a cadence of two days; the SEDs for the pure deflagration models start 1 day after explosion, with a cadence of one day. All Phoenix SEDs are binned in about 1000 irregularly spaced wavelength bins with an average width of 25 Å. As discussed in Section 2.3, the Poisson uncertainty on the fluxes plays almost no role in the light curve fits and was set to a small number.

Finally, we generate mock light curve observations of the explosion models by multiplying their SEDs with filter transmission functions representing either the Bessell filter system (*UBVRI*; Bessell 1990) or the SDSS filter system (*ugriz*; Fukugita et al. 1996). This operation is performed using the publicly available Supernova Analysis software (SNANA; Kessler et al. 2009). The mock observations are generated with a cadence of one day, and at a very low redshift of $z = 0.002$ so that K-corrections are unnecessary.

2.2. The SALT2 Data-driven Model

With light curves for a given explosion model in hand, the simplest comparison with observations is to pick one or a few well-observed SNeIa, and overplot their light curves. However, SNIa light curves are heterogeneous, and picking one or a few is inevitably a biased representation of light curves as a whole. Fortunately, the observational community has developed interpolation models, called “data-driven models”, in order to standardize the brightness of each SNIa. They generally constitute complex functions for the spectral evolution of SNeIa with a few free parameters which are determined from a least-squares fit to light curves. All other degrees of freedom (i.e., the exact shape of the epoch-wavelength surface) are fixed by training the model on large sets of observed events. Thus, data-driven models summarize information from many SNeIa, and allow a much more robust estimation of light curve characteristics than comparing to a few hand-picked SNeIa. A drawback of using data-driven models is that they are trained on normal SNeIa, meaning they do not capture peculiar SNIa events.

For the purposes of this analysis, we choose the Spectral Adaptive Light curve Template method (SALT2; Guy et al. 2005, 2007, 2010, hereafter G10). SALT2 fits broadband photometric light curves using a stretch-dependent SED for each epoch, and a color law. The model is agnostic as to the physical mechanisms which cause decline rate and color variations in SNeIa. A plethora of other light curve models exists in the literature, almost all of which could be used instead of SALT2. For example, SiFTO (Conley et al. 2008) is similar to the SALT2 model, but uses the SED of Hsiao et al. (2007). The Multicolor Light Curve Shapes method (mlcs2k2; Riess et al. 1996a; Jha et al. 2007) is built on the underlying assumption that all color variations are due to dust reddening similar

to that in our own galaxy. SNooPy (Burns et al. 2011) was especially designed for infrared (IR) light curve fitting, and could be used to extend our analysis into the infrared (given reliable IR light curves from explosion models).

We choose the SALT2 model as it is publicly available and has been trained on the most recent SNLS3 sample (G10). Since we use the model extensively in this analysis, we review its main features here. SALT2 models the flux as a function of wavelength, λ , and time, t , such that

$$F(t, \lambda) = x_0 [F_0(t, \lambda) + x_1 F_1(t, \lambda)] \times e^{c \times CL(\lambda)}. \quad (1)$$

The spectral surfaces F_0 and F_1 , as well as the color law $CL(\lambda)$, are functions with thousands of parameters, all of which are fixed by “training” the model on observed data. The remaining parameters, x_0 , x_1 and c , are derived from a least-squares fit to an individual SNIa event, where light curves in all filter bands are fit simultaneously (using the nominal SALT2 model errors which include a covariance term). Since we refer to these quantities frequently, we shall briefly review their physical meaning. Though the fitted parameter x_0 is a flux normalization rather than a magnitude, we will generally refer to the corresponding magnitude

$$m_B = -2.5 \log_{10}(x_0) - 10.095. \quad (2)$$

As evident from Equation (1), x_1 is the coefficient of the second flux surface F_1 , rather than a simple stretch quantity, s , in the sense of the original SALT model ($t \rightarrow t/s$). However, the main component of F_1 does correspond to the difference of light curves with different stretch values, so that there are nearly linear relations between x_1 and s (Guy et al. 2007), as well as between x_1 and Δm_{15} . Thus, we will refer to x_1 as stretch. Lastly, c is the coefficient of the color law of Equation (1), and is virtually equal to $B - V$ color (Kessler et al. 2013),

$$B - V = 1.016c + 0.0008x_1 + 0.0232. \quad (3)$$

Due to these close relationships with observable quantities, we shall speak of the SALT2 parameter space as a stretch–color–magnitude space. In the rest of this paper we refer to the stretch, color and magnitude derived from a light curve fit interchangeably as fitted parameters, fit results, or simply parameters.

Though SALT2’s spectral training covers wavelengths from 2000 Å to 9200 Å, the central wavelengths of filter bands are not recommended to lie beyond 2800 Å and 7000 Å. We adhere to this standard by using *UBVR* and *ugr*. The central wavelength for the next set of filters, *I*-band and *i*-band, lie beyond 7000 Å. Extending filters past the recommended wavelength range would introduce uncertainties of a few percent which would be acceptable for the purpose of fitting explosion models, since they typically deviate from the SALT2 light curves by a larger amount anyway. However, computing reliable radiative transfer results in the IR has traditionally been challenging because the results are highly sensitive to the ejecta temperature (see, e.g., Kasen 2006). Thus, we refrain from including *I*-band in our comparisons. Our method, however, can easily be extended to include the IR.

So far, we have discussed the necessary background for performing light curve fits and deriving x_1 , c and m_B . In Section 2.4 we will also derive a population model for those parameters, and thus be concerned with the *correlations* between the populations in each parameter. SALT2 models the correlation between stretch and peak brightness with a parameter α , and

the correlation between color and peak brightness with a parameter β . In addition, a magnitude offset M_0 allows us to translate to absolute magnitudes (Guy et al. 2007). The three additional parameters are *not* derived from the light curve fit, but in a second, independent fit which, given a certain set of observed SNeIa, minimizes the scatter in the Hubble diagram. For each SNIa in the set, the distance modulus is estimated as

$$\mu_{\text{est}} = m_B - M_0 + \alpha x_1 - \beta c \quad (4)$$

where x_1 , c and m_B are derived from the light curve fit, and M_0 , α and β are determined by the Hubble diagram fit (see, e.g., Marriner et al. 2011). Thus, the results for M_0 , α and β depend on the sample of SNeIa used for the Hubble diagram fit, and their values may vary between surveys (see Section 4.1). It is important to note that using SALT2 for our light curve fits does *not* force us to adopt the model of Equation (4) when describing the correlations between stretch, color and magnitude. It is, however, by far the most intuitive and well described way to use the results of SALT2 light curve fits to describe those correlations, and we thus adopt it.

For explosion models, we can simplify Equation (4) since we know the true distance modulus μ at which the mock observations were generated. We translate the observed magnitude into an absolute magnitude, $M_B = m_B - \mu$, giving an expression for the absolute magnitude we expect a SNIa to have based on its stretch and color,

$$M_B = M_0 - \alpha x_1 + \beta c. \quad (5)$$

We note that M_B represents the best-fit peak magnitude based on light curves in all filter bands, and is not the magnitude of the *B*-band at the epoch of peak brightness. Furthermore, the relation between M_B and m_B , and thus Equation (5), are only valid at $z = 0$. Since we generate the mock light curves of our explosion models at a negligible redshift, this caveat does not pose a problem. We describe how we derive M_B for higher redshift data in Appendix A.4.

2.3. Fitting Explosion Model Light Curves

The goal of fitting simulated light curves to a data-driven model is to estimate the likelihood that the underlying explosion model could represent an observed SNIa. Accepting the paradigm that SNIa light curves are described by an analytical function with a few free parameters (x_1 , c and m_B , in the case of SALT2), we split this likelihood into two separate components. First, the quality of the fit itself indicates whether the synthetic light curves represent a SNIa. Secondly, the resulting best-fit values for x_1 , c and m_B correspond to a likelihood of observing a SNIa with those values. The second part will be discussed in Section 2.4, while this section deals with how the SALT2 model is used to fit explosion model light curves rather than observed SNeIa.

In the ordinary case of fitting observed data, a light curve fit refers to a least-squares fit of a set of given SNIa observations to Equation (1), redshifted into the observer frame and multiplied by the filter bands used in the observations. We use the SNANA light curve fitting program to apply the same procedure to our mock observations of explosion models. However, there are some differences between explosion models and observed data which deserve further discussion before we describe the more technical aspects of the fitting procedure.

When we fit explosion model light curves, SALT2 takes on the role of “the model” while the simulated light curves serve as “the data”. Of course, the simulated light curves

do not carry the measurement uncertainties typically associated with SNIa observations. In order to follow the model-data approach faithfully, we could use SNANA to simulate the survey conditions of, say, SDSS, and generate mock observations at a variety of redshifts, introduce reddening and atmospheric conditions, and propagate them through a virtual telescope, camera and processing pipeline. Such mock observations would then carry flux uncertainties similar to those of the survey which was simulated. There are, however, two reasons not to follow this procedure. First, we would inevitably introduce selection biases, and discard information about the explosion model light curves. Secondly, the simulated statistical uncertainties would carry no information about the systematic uncertainties of explosion models, which are much larger than the typical statistical uncertainties in the data.

The systematic uncertainties can be split into two categories, parametric and non-parametric errors. Parametric sources of error include the progenitor’s mass and C/O abundance ratio, and the number, locations and sizes of the ignition bubbles. Non-parametric systematic errors are caused by missing or uncertain physics, for example in the flame model, the detonation model, the energy deposition of gamma rays, the ray tracing algorithm, or the number and properties of spectral lines in the radiation transfer calculation. More mundane sources of systematic errors include inadequate spatial and temporal resolution in the explosion or radiation transfer phase, an inadequate number or distribution of Lagrangian tracer particles used to determine the abundance of elements, or an inadequate number of rays, spectral bins, or angular bins in the radiation transfer phase. Unless the simulated survey conditions are extremely poor, a combination of all those sources of systematic uncertainty far outweighs the statistical errors.

As systematic errors typically dominate over statistical uncertainties, and because we wish to avoid discarding light curve information by simulating survey conditions, we choose to ignore statistical uncertainties entirely. Instead, we place the simulated SNeIa at a low redshift and set their statistical uncertainties to a small number, ensuring that the uncertainties on the SALT2 model dominate the error term in the χ^2 computation. This strategy has two significant consequences. First, the χ^2 per degree of freedom (χ^2_ν) of the light curve fits is generally much greater than for observed data. Secondly, we cannot interpret the results of the SALT2 fits in a statistically meaningful fashion. For example, while $-\chi^2/2$ from the fit to a set of observed SNIa light curves is ordinarily interpretable as the log-likelihood of the event having been a SNIa, we do not assign such interpretation to an explosion model.

While the lack of rigorous error treatment may be a sobering realization, we are not trying to compute the likelihood of a certain model representing a SNIa, but rather we are solving an optimization problem. We are trying to identify which explosion models, or which classes of explosion models, come closest to reproducing the light curves of real SNeIa. Our methodological approach can yield information about the values of the model parameters that are favored and disfavored given the current sample of observed SNeIa. It can also provide clues as to non-parametric sources of systematic error. For these purposes, we do not need to derive an absolute likelihood. Thus, we shall avoid quoting quantities which are usually assigned statistical meaning, such as χ^2_ν , and instead focus on indicators of light curve quality which can be computed without invoking uncertainties on the light curves themselves.

Having decided to forego a statistical interpretation of the

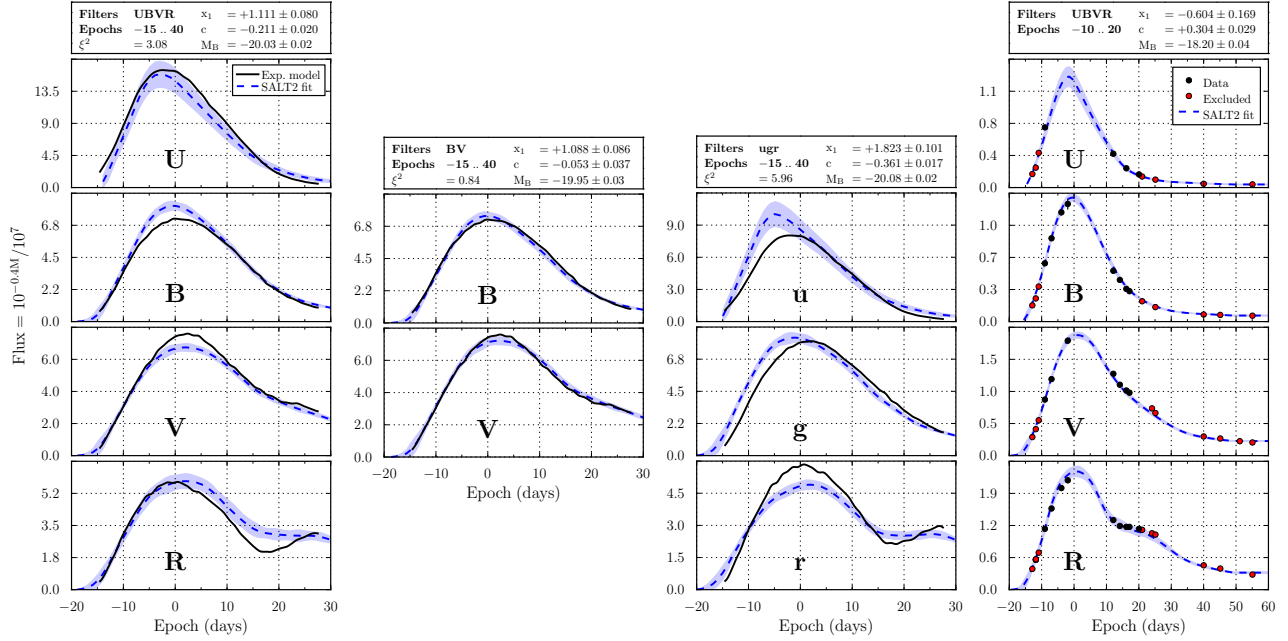


Figure 2. The influence of filter band choice on SALT2 fit results. Each of the left three columns represents a fit to the same explosion model, but using different filter bands. The choices of filters and epoch range, as well as the fit results, are indicated in the top panels. The black curves show the 68° viewing angle of the KRW09_asym_6_dc_2 model. All fits include epochs between -15 and $+40$ days, which includes all epochs of this viewing angle. The dashed blue curves show the SALT2 fits, with shaded blue regions indicating the 1σ confidence regions of the SALT2 model. The three columns correspond to three different choices of filters (*UBVR*, *BV* and *ugr*), demonstrating that this choice can influence the fit results, particularly when the fit is not very good. In the *UBVR* fit, the SALT2 model overestimates the *B*-band peak magnitude, and underestimates the *V*-band peak. In the *BV* fit, the peak magnitudes of the *B* and *V* bands can be fit simultaneously, resulting in a significantly redder color ($c = -0.05$ instead of -0.21). The *ugr* fit, however, results in a bluer color than *UBVR* ($c = -0.36$). Right column: *UBVR* fits to the observed SN 2002bo (CfA3 data, see Appendix A.2). Even though epochs before -10 and after $+20$ days are excluded from the fit, the fit is compatible with the data at all epochs.

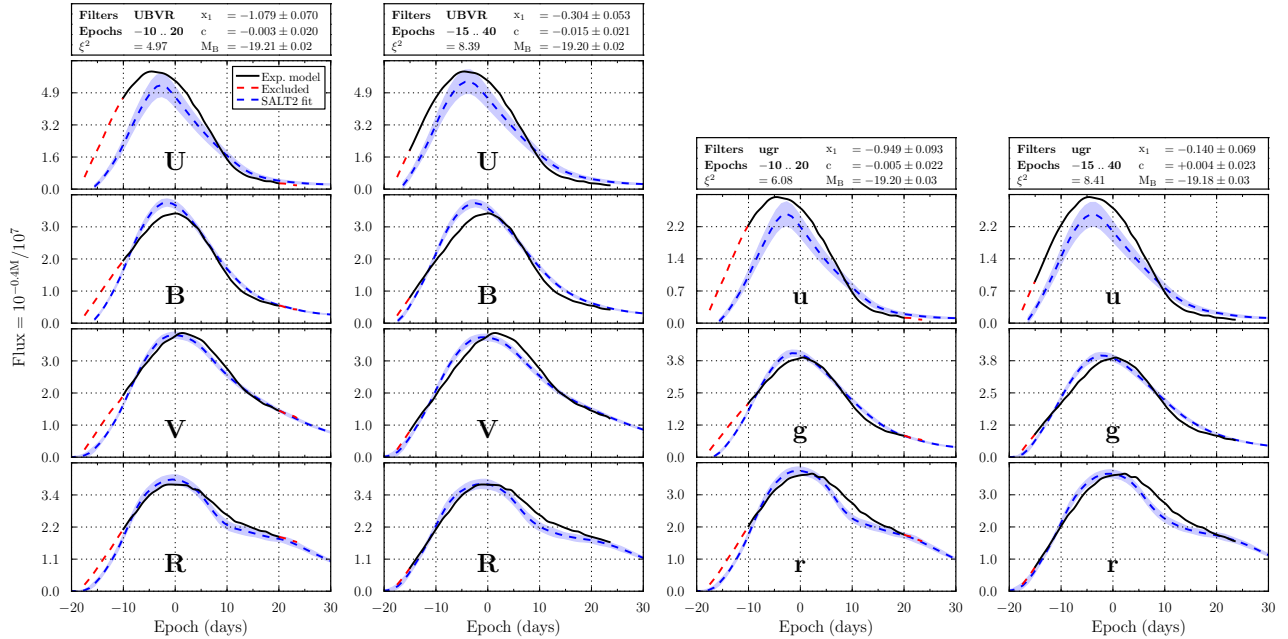


Figure 3. Same as Figure 2, but for different fitted epoch ranges. The light curves show the 15° viewing angle of the KRW09_iso_6_dc_4 model. In the left column, only epochs from -10 to $+20$ days from *B*-band peak brightness were included in the fit, as indicated by the dashed red, excluded regions. In the second column, early and late epochs were included as well (-15 to $+40$ days), significantly degrading the fit as the SALT2 model cannot accommodate the shallow rising slope of the light curves. While the color and magnitude results of the two fits are almost identical, the stretch varies dramatically from ≈ -1 to ≈ -0.3 . The same is true when the *ugr* filters are used instead of *UBVR* (right two columns), with the stretch varying from ≈ -0.95 to -0.14 . Note that the main reason for the large discrepancies is that the light curve fit is relatively poor in the first place, at least when the early epochs are included.

light curve fits, we face another issue which causes systematic uncertainty in the fit results. We need to make certain choices regarding the light curve fits, two of which turn out to influence the results significantly: the choice of filter bands, and the epoch range included in the fit. Figure 2 demonstrates the impact of the first choice. Adding or omitting filter bands can change the fit results, as shown by the first two columns in Figure 2. While fitting the entire *UBVR* set analyzes a larger wavelength range, fits to a subset may result in more accurate fits to those bands. For example, fits to *BV* only (center column of Figure 2) might lead to a better estimate of *B*–*V* color or *B*-band peak brightness. Furthermore, there is no clear reason to prefer, for example, the Bessell filter system (*UBVR*) over the SDSS system (*ugr*), but they result in slightly different fitted parameters (third column of Figure 2). Especially the color parameter, *c*, is affected by the choice of filters, since it correlates closely with *B*–*V* color (Equation (3)).

Secondly, the fit results can depend on the choice of fitted epoch range, particularly when the light curve fit is poor, as demonstrated in Figure 3. A simple argument could be made that one should always include as many epochs as possible, if the radiative transfer code provides them. In practice, however, that is not the best choice. First, the early and late epochs can contribute a disproportionate amount of χ^2 per epoch. This emphasis appears when an explosion model fails to match the rising or falling slope, since the flux uncertainties on the SALT2 model are small at early and late times (though the magnitude errors are quite large). While such disagreement highlights a real problem with the explosion model, it can drive the fit away from the best fit around peak. In principle, an explosion model should of course be able to reproduce observed light curves at all epochs, but almost no explosion model to date has reached this level of agreement with data. Secondly, one might be interested in the performance of a particular explosion model around peak, not at early or late times. Third, when comparing explosion models we do not wish to penalize a model for going out further in time than others. Such a χ^2 penalty would inevitably occur if the fitted epoch range was varied between models.

The biasing of fit results due to our choices of filter bands and epoch range is expected, since those choices simply correspond to weighting certain regions of the epoch-wavelength surfaces stronger than others. For explosion models which perfectly fit the SALT2 light curves, however, we expect no such bias. We tested this assumption by generating ideal light curves from the epoch-wavelength surfaces of the SALT2 model, and then fitting them with SALT2. As expected, fits to these ideal light curves reproduced the input magnitude, stretch and color to better than 0.1% error, regardless of which epoch range or filter bands were fit. As a second check, we tested the impact of epoch range on the fitted stretch parameter when fitting observed data. Since data are measured in one particular filter system (e.g., *UBVRI*), we cannot test the impact of using other filter systems (e.g., *ugriz*). We chose two small sets of events from the CfA3 survey (Appendix A.2) which have data points before -10 and after $+20$ days. The first set was chosen to contain only very good fits with $\chi_v^2 \approx 1$, while the second set consisted of SNeIa with relatively poor fits, $\chi_v^2 > 1$, such as the sub-luminous 2005hk. All events except 2005hk were part of the SALT2 training set (G10). When fitted with different epoch ranges and subsets of filters, the fitted parameters for the set with good fits show very little variation (typically about $0.1 \sim 0.2$ in the stretch parameter x_1 , corresponding to a $0.01 \sim 0.02$ correction in peak mag-

nitude). For example, the light curve fit to 2002bo (shown in the right column of Figure 2) is compatible with the data at all epochs, even though epochs before -10 and after $+20$ days were excluded from the fit. The differences between fits of the poorly fit set were about twice as large as for the well-fit set, as expected. However, even the poorly fit set shows modest variations with epoch range compared to many explosion models (Section 3). This test demonstrates once again that the results of high-quality light curve fits are less sensitive to the fitted epoch range than the results of poor fits. Since observed data generally fit much better than explosion models, their fitted parameters change relatively little when changing the fitted epoch range.

In conclusion, the choice of filter bands and epoch range systematically bias the results of light curve fits to explosion models which are not well fit by SALT2. The choice of filter bands has a particularly strong impact on color, and the epoch range on stretch. The peak brightness is generally less sensitive to the details of the fitting procedure. Since there is no clear choice, we fit models with a wide range of reasonable filter and epoch range choices. Here, we fit each light curve with three sets of filters (*UBVR*, *BV* and *ugr*) as well as four epoch ranges (-10 to $+20$, -10 to $+40$, -15 to $+20$ and -15 to $+40$), resulting in a total of 12 fits. The three sets of filter bands allow us to fit the maximum wavelength range (*UBVR*), get the best fit to the well-constrained *B* and *V* bands (*BV*), and investigate an alternative filter system (*ugr*). The set of epoch ranges was chosen to include and exclude the regions of -15 to -10 days, and $+20$ to $+40$ days, since many explosion models struggle to match the SALT2 model at those epochs. While the SALT2 model is defined to -20 days, the data coverage becomes sparse at such early times. Furthermore, many explosion model light curves do not include epochs before -15 days.

The dispersion in the fitted parameters x_1 , c and m_B from the 12 fits is interpreted as a systematic uncertainty on those parameters. As outlined above, this dispersion is generally larger for explosion models which are poorly fit in the first place, meaning that the results are better constrained for explosion models which agree best with data. This correlation is reassuring, since we care somewhat less about how poorly a model fits the data, but *do* care in cases where the model fits the data well.

Finally, we wish to define a goodness-of-fit parameter for a light curve fit. As discussed above, χ_v^2 cannot be interpreted in the usual statistical context, since, in the absence of uncertainties on the explosion model, the formal χ_v^2 gives a small likelihood for any of the light curve fits in this analysis. Thus, we define a χ_v^2 -like goodness-of-fit parameter,

$$\xi^2 \equiv \frac{1}{N} \sum_{i=1}^N \left(\frac{F_{i,\text{model}} - F_{i,\text{SALT}}}{\sigma_{i,\text{SALT}}} \right)^2 \quad (6)$$

where N is the number of epochs, F_i the flux at epoch i , and $\sigma_{i,\text{SALT}}$ the uncertainty on the SALT2 model at that epoch. The main differences between ξ^2 and χ_v^2 are that ξ^2 is agnostic of uncertainties on the explosion model light curves, and that it ignores the covariances between the fitted parameters. Thus, we once again emphasize that no statistical interpretation should be derived from the value of ξ^2 .

2.4. SNIa Population in Color–Stretch–Magnitude Space

In the previous step, we quantified the agreement between explosion model light curves and the SALT2 model, indicat-

Table 1
Parameters for the Population Model of SNe in $x_1 - c - M_B$ Parameter Space

Parameter	Value	Description	Reference
α	0.13	Slope of $M_B - x_1$ relation (derived from Hubble diagram fit)	Conley et al. (2011); Sullivan et al. (2011)
β	3.2	Slope of $M_B - c$ relation (derived from Hubble diagram fit)	Conley et al. (2011); Sullivan et al. (2011)
M_0	-19.095	Uncorrected B -band peak magnitude (derived from Hubble diagram fit)	Guy et al. (2010)
H_0	70 km s ⁻¹ Mpc ⁻¹	Hubble constant (degenerate with M_0)	Guy et al. (2010)
σ_M	0.13	Intrinsic scatter in M_B (including uncertainty in H_0)	Kessler et al. (2013)
μ_{x1}	0.5	Mean of distribution in x_1	Kessler et al. (2013)
σ_{x1-}	1.4	Standard deviation for $x_1 > \mu_{x1}$	Kessler et al. (2013)
σ_{x1+}	0.7	Standard deviation for $x_1 < \mu_{x1}$	Kessler et al. (2013)
μ_c	0	Mean of distribution in c	Kessler et al. (2013)
σ_{c-}	0.08	Standard deviation for $c > \mu_c$	Kessler et al. (2013)
σ_{c+}	0.13	Standard deviation for $c < \mu_c$	Kessler et al. (2013)
$w_{c,2}$	0.04	Weight of secondary distribution in c	This paper
$\mu_{c,2}$	0.3	Secondary distribution: mean in c	This paper
$\sigma_{c-,2}$	0.2	Secondary distribution: standard deviation for $c > \mu_{c,2}$	This paper
$\sigma_{c+,2}$	0.2	Secondary distribution: standard deviation for $c < \mu_{c,2}$	This paper
$w_{M,2}$	0.04	Weight of secondary distribution in M_B	This paper
$\mu_{M,2}$	-19.095	Secondary distribution: mean in M_B	This paper
$\sigma_{M,2}$	0.35	Secondary distribution: standard deviation for M_B	This paper

Note. — The quoted value for M_0 given in G10 refers to the SiFTO light curve fitter rather than SALT2. Because SiFTO has different corrections for color and stretch, the uncorrected magnitude M_0 is slightly different, but can be converted to the SALT2 value using linear transformations (J. Guy 2012, private communication). The corresponding value of H_0 used in their analysis is 70 km s⁻¹ Mpc⁻¹. See Section 4.1 for a detailed discussion.

ing whether they represent a Type Ia-like explosion. However, there are three free parameters in the SALT2 fit, x_1 , c and m_B . Even if the light curves in question are well fit with the SALT2 model, there is no guarantee that the resulting parameters correspond to values observed in nature. Namely, the explosion model could suffer from physically unreasonable color and stretch properties, or not obey the magnitude–stretch and magnitude–color relations. Furthermore, we wish to evaluate the likelihood that a certain set of fit parameters could be observed in nature. Hence, we need a model for the population of SNeIa in the $m_B - x_1 - c$ parameter space. In the context of SALT2, x_1 and c are independent parameters, whereas the peak magnitude is correlated with x_1 and c . Thus, generating a population model consists of two somewhat independent steps: quantifying the observed distributions of stretch and color, and quantifying the relations between stretch, color and magnitude.

The observed distributions of x_1 and c have been quantified for various surveys, but surveys are subject to significant observational biases. Here we are interested in the *underlying* distribution of x_1 and c , corresponding to the results of an ideal, unbiased survey. These unbiased distributions were modeled by Kessler et al. (2013, hereafter K13), who determined the distributions by comparing Monte-Carlo simulations with survey data. The Monte-Carlo simulations, run using SNANA, assumed a certain parent population in stretch and color, and forward-modeled various observational biases. These effects included an improved signal-to-noise model and the corresponding cuts, Malmquist bias, search efficiency, as well as the efficiency of the spectroscopic selection. The most likely underlying population was determined by matching the results of the simulation with the observed distributions of 251 SNeIa from the SDSS (Appendix A.1) and 191 SNeIa from the Supernova Legacy Survey (SNLS; Astier et al. 2006, G10). The underlying populations were modeled as asymmetric, continuous Gaussians such that for a parameter

$$\theta = (x_1, c),$$

$$\frac{dP(\theta)}{d\theta} = \sqrt{\frac{2}{\pi}} \frac{1}{(\sigma_{\theta+} + \sigma_{\theta-})} \begin{cases} \exp\left(\frac{(\theta - \mu_\theta)^2}{2\sigma_{\theta+}^2}\right) & \forall \theta > \mu_\theta \\ \exp\left(\frac{(\theta - \mu_\theta)^2}{2\sigma_{\theta-}^2}\right) & \forall \theta < \mu_\theta. \end{cases} \quad (7)$$

Table 1 shows the values for μ_θ and the various standard deviations used, as determined by K13.

Having quantified the distributions of stretch and color, we now move on to their correlations with magnitude. In Section 2.2 we described how the SALT2 model deals with the relations between x_1 , c , m_B , and M_B using the parameters M_0 , α and β which are derived from a Hubble diagram fit. Since explosion models are not guaranteed to follow the relations between stretch, color and magnitude observed in nature, we do not use a set of explosion models to derive M_0 , α and β . Instead, we pick sensible values derived from large SNIa surveys (Table 1). We discuss these choices in detail in Section 4.1.

Equation (4) suggests that the fitted m_B (and thus M_B) is perfectly correlated with x_1 and c , and assumes no residual scatter in the Hubble diagram which is unrealistic. Thus, we add a scatter term, Δ_M to the absolute magnitude, giving the final relation

$$M_B = M_0 - \alpha x_1 + \beta c + \Delta_M \quad (8)$$

where Δ_M is assumed to be drawn from a symmetric Gaussian distribution with mean zero and standard deviation σ_M . The standard deviation includes both the intrinsic scatter as well as the uncertainty of the Hubble constant, which is a subdominant but relevant contribution. We are now in a position to write down the probability density of SNeIa in the 3D space of stretch, color and absolute magnitude. The probability distribution is the product of three independent Gaussians in x_1 , c and Δ_M , and can easily be transformed from the magnitude scatter Δ_M to absolute magnitude,

$$dP(x_1, c, M_B) \propto e^{\frac{1}{2}\chi^2} dx_1 dc dM_B \quad (9)$$

with

$$\begin{aligned}\chi^2 &= \frac{(x_1 - \mu_{x_1})^2}{\sigma_{x_1}^2} + \frac{(c - \mu_c)^2}{\sigma_c^2} + \frac{\Delta_M^2}{\sigma_M^2} \\ &= \frac{(x_1 - \mu_{x_1})^2}{\sigma_{x_1}^2} + \frac{(c - \mu_c)^2}{\sigma_c^2} + \frac{(M_B + \alpha x_1 - \beta c - M_0)^2}{\sigma_M^2}\end{aligned}$$

where σ_{x_1} and σ_c are understood to take on different values above and below the respective means of their distributions. We note that all σ denote the widths of the population distributions rather than fitted errors. A more formal and general derivation of this result is given in Appendix B.

Figure 4(a) shows confidence contours for the likelihood of Equation (9). Each panel shows the contours in two variables, marginalized over the third variable. Note that in the cases of the $x_1 - M_B$ and $c - M_B$ planes, the marginalization over asymmetric Gaussian distributions leads to a 2D probability which itself is not Gaussian any more. Expressions for the probability density shown in Figure 4 are given in Appendix B.

To check that our population model differs from biased survey data in ways which we expect and can explain, we overplot data from the SDSS survey in Figure 4(a). We review the SDSS survey, the cuts applied to the sample, and our procedure for estimating the rest-frame peak magnitude in Appendix A. The differences between the overplotted SDSS data and the population model clearly demonstrate why simply comparing the fit results from explosion models to those of survey data would be inappropriate. The SDSS data is strongly biased toward blue SNeIa (low c) and slow decliners (high x_1), which are synonymous with bright events (Malmquist bias). All outliers are compatible with the 3σ confidence contours, at least within their 1σ error bars.

However, there is one potential issue with the population model derived from SDSS and SNLS data. From the survey data used to determine the x_1 and c distributions (see Figures 1 and 2 in K13), one might suspect that the dim ends (red, fast decliners) of these distributions are poorly constrained. In order to investigate these regions of parameter space, we turn to a low-redshift survey, the CfA3 sample of nearby SNeIa (reviewed in Appendix A.2). The CfA3 sample was not considered in the original population model since its survey biases could not be modeled as accurately as those of SDSS and SNLS, but it contains a higher fraction of red, dim events. Thus, the CfA3 survey should be ideal for the purpose of finding outliers in the SNIa population. In addition, we use the well-observed set of SNeIa used in Jha et al. (2007), and refer to the combined sample as the nearby sample. Figure 4(b) shows the nearby sample plotted over the contours of our population model. The comparison demonstrates that the nearby sample contains some objects which lie significantly outside the $x_1 - c$ range expected from the population model of K13 (with a sample of this size, there should be zero or one objects outside the 99.7% contour). In particular, there appears to exist a very red population not represented by the population model. Secondly, the $x_1 - M_B$ plot suggests that there are objects with both brighter and dimmer magnitudes than expected. The cuts described in Appendix A.3 ensure that the extreme fit results are not artifacts of poor light curve fits. However, we cannot exclude the possibility that at least a fraction of the red, dim SNeIa experienced significant host galaxy reddening. Nevertheless, as long as there is a possibility that the red colors and dim magnitudes are intrinsic, the popula-

tion model should not exclude explosion models with similar characteristics.

To account for the tails in the SNIa population, we extend the population model to include a second Gaussian, making up 4% of the overall population, in both c and M_B . The means and standard deviations for the secondary populations are listed in Table 1. The second Gaussian in color is centered at $c = 0.3$, with $\sigma = 0.2$, adding a total 1.3% likelihood for a SNIa to be observed with a value of c greater than the previous 3σ limit of $c = 0.39$. Since the second Gaussian is centered at red colors, it adds virtually no probability where $c < 0$. The second Gaussian in M_B is centered at the original value of M_0 , and thus simply allows for an outlier population at low and high magnitudes, adding a total of 0.5% likelihood each above and below the previous 3σ limits. Contrary to color and magnitude, Figure 4(b) shows no evidence for an extreme population in x_1 . Figure 4(c) demonstrates that the extended population model does a better job of accounting for the extreme objects of the nearby sample. Figure 5 shows the same extended population model, for the corrected magnitude, $M_B + \alpha x_1 - \beta c$, instead of M_B . The advantage of this variable transformation is that the Gaussians are independent in all three variables, and it is thus easier to see which parts of the 3D parameter space are allowed. The plots of M_B can be somewhat misleading, since they show projected confidence contours, not the 3D likelihood. A more detailed mathematical description of the population model is given in Appendix B.

Furthermore, we note that the contours in the $x_1 - M_B$ plane of Figure 4(c) indicate a less tight correlation between stretch and peak magnitude than the Phillips relation between Δm_{15} and M_B (see, e.g., Figure 1 of Hillebrandt et al. (2013) or Figure 7 of Blondin et al. (2011)). There are a few reasons for the weaker correlation. First, tight Phillips relation fits are often derived from *color-corrected* peak magnitudes (e.g., Folatelli et al. 2010), while Figure 4(c) shows uncorrected magnitudes. Removing the component of the scatter in magnitude which is correlated with color reduces the scatter in the stretch–magnitude relation significantly. Secondly, our extended population model accounts for dim objects which have been shown to lie off the main Phillips relation (Foley et al. 2013). Finally, the stretch parameter x_1 is derived from an entire set of light curves, rather than two particular epochs in B -band, and there is no reason to assume that its correlation with peak magnitude would be as tight as that of Δm_{15} .

While the extended population model seems to do well at describing the nearby sample, we emphasize that the purpose of the extension is *not* to make accurate statements about the actual, underlying population of SNeIa, since it was not derived from data in a rigorous fashion. Given the scarcity of current data, such an investigation will be a future project (see Section 4.1). Here, we simply make sure to include explosion models with extreme fitted parameters if there are *any* reasonably well observed events with similar parameters. Adding secondary populations with a few percent of the overall population changes the likelihood closer to the peak of the distribution very little. In the context of comparing explosion models to the population model, the extended model only differs from the basic model when the fit results are somewhat extreme. The validity of our population model is further discussed in Section 4.1.

2.5. Figure of Merit

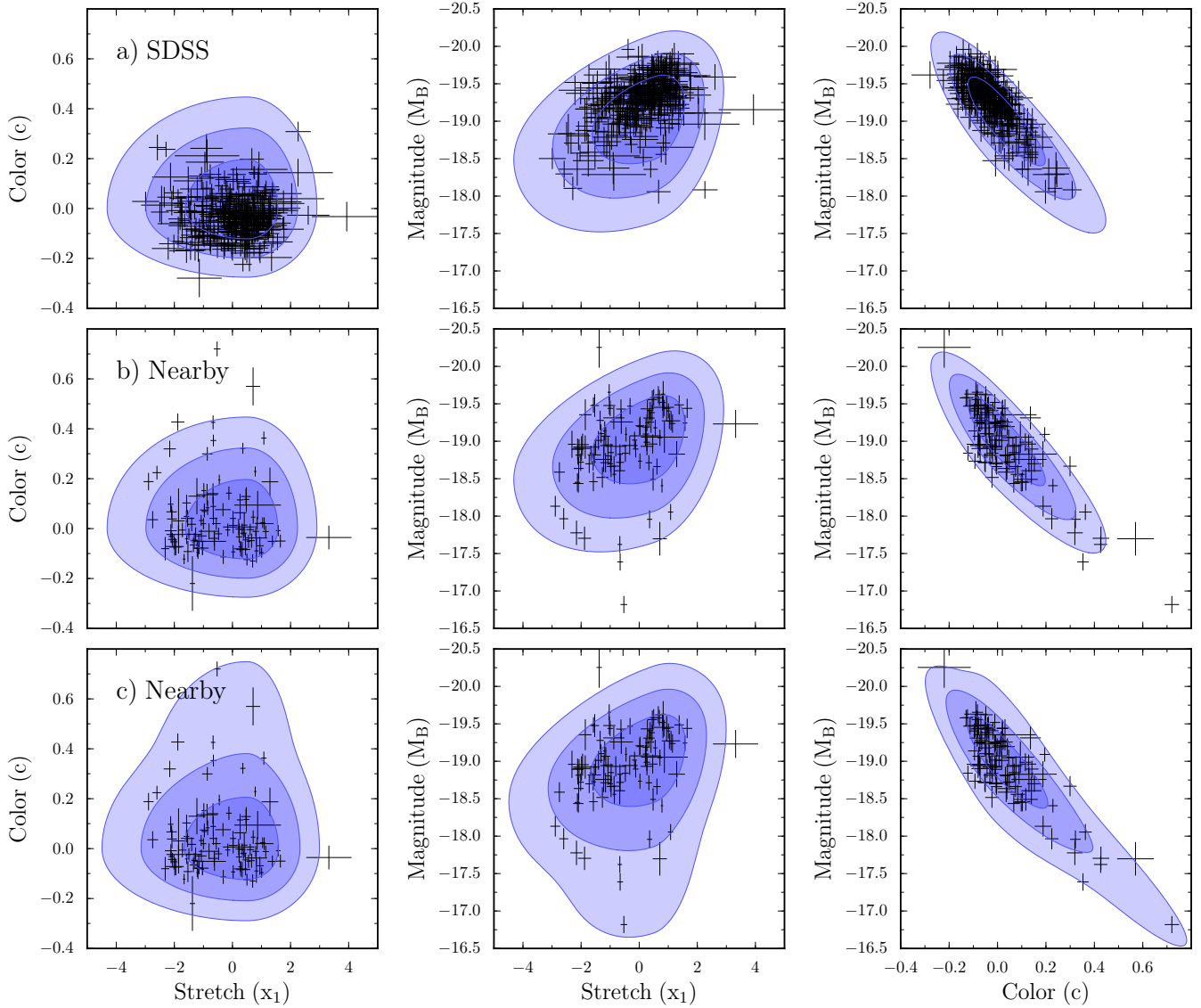


Figure 4. Constructing a population model. Each row shows confidence contours (68.3%, 95.4% and 99.7%) in $x_1 - c$, $x_1 - M_B$ and $c - M_B$ space, marginalized over the third variable which is not plotted. Row (a): the population model of Kessler et al. (2013), with survey data from SDSS. The comparison demonstrates the necessity of a population model, since the survey data are highly biased toward blue (low c), slow-declining (high x_1) events. Row (b): the nearby sample contains outliers which should not exist according to the population model. Row (c): the extended population model does a better job accounting for the nearby outliers (see Section 2.4 for details).

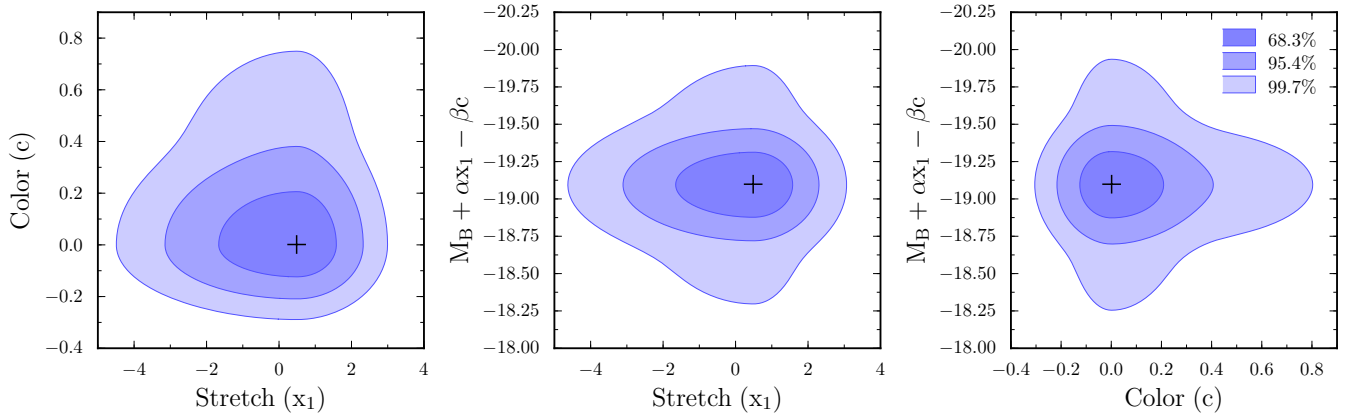


Figure 5. The extended population model as in Figure 4(c), but plotting the corrected magnitude instead of M_B . In corrected magnitude space, the basic population model consists of three independent Gaussians, and it is easier to visually evaluate how likely an event is according to the model. The black crosses mark the loci of maximum probability density.

In the last two sections we described procedures for fitting explosion models with SALT2, and derived a goodness-of-fit indicator ξ^2 as well as a likelihood of the fit results corresponding to values observed in nature. We now wish to merge these two components into one figure of merit, f , which represents a weighted sum of its two constituents. Of course, there are countless ways to define f , meaning any procedure is somewhat arbitrary and can be changed for any particular purpose. Here, we aim to assign equal weight to both the goodness-of-fit and the likelihood of fit parameters.

For a given set of fitted parameters, we define p to be the fraction of the population with a *lower* likelihood of being observed in nature than the set of fit parameters in question. This definition means that $p = 1$ corresponds to x_1 , c and M_B at the point of highest likelihood, and, for example, $p = 0.01$ indicates that only 1% of observed SNeIa have parameter values more extreme than those at hand. It makes sense to put a lower limit on the figure of merit for p because the population model is not defined at very low likelihoods, and the computation can return 0 due to round-off error. Furthermore, we re-normalize the figure of merit to take on values between 0 (worst) and 1 (best) to simplify its interpretation. We thus define

$$f_p \equiv \begin{cases} \frac{\log_{10}(p_{\min}) - \log_{10}(p)}{\log_{10}(p_{\min})} & \forall p \geq p_{\min} \\ 0 & \forall p < p_{\min} \end{cases} \quad (10)$$

Similarly, we need to define a ξ_{\max}^2 above which we consider a light curve fit to have failed. Incidentally, some light curves fit so poorly that the fit fails within SNANA, and we penalize such failed fits by assigning them $\xi^2 = \xi_{\max}^2$. In either case, failed fits are not included when computing f_p , since they contain no information about the best-fit parameters. Furthermore, we assign ξ_{\max}^2 to certain *epochs* (not entire fits) if both the flux and uncertainty of the best-fit SALT2 model go to zero. In this rare case, ξ^2 for the epoch is not well-defined (see Equation (6)).

While p is automatically limited to $p \leq 1$, there is no clear lower limit for ξ^2 . A ξ^2 below 1 corresponds to a set of light curves which, on average, lie within the statistical uncertainty of the SALT2 model. Such an excellent match is achieved by a few individual fits to the explosion models considered here, but no model achieves $\xi^2 < 1$ when averaged over the 12 sets of fits with different filters and epoch ranges. Nevertheless, we wish to ensure that f_{ξ^2} has both lower and upper bounds, and thus define

$$f_{\xi^2} \equiv \begin{cases} 1 & \forall \xi^2 < 1 \\ \frac{\log_{10}(\xi_{\max}^2) - \log_{10}(\xi^2)}{\log_{10}(\xi_{\max}^2)} & \forall 1 \leq \xi^2 \leq \xi_{\max}^2 \\ 0 & \forall \xi^2 > \xi_{\max}^2 \end{cases} \quad (11)$$

All the information about the quality of the light curve fits and the fitted parameters is contained in f_{ξ^2} and f_p . In order to rank explosion models by their quality, we wish to combine these two figures of merit into an overall figure of merit, f , which we define to be a weighted sum of f_p and f_{ξ^2} , with weights w_p and w_{ξ^2} . As both f_p and f_{ξ^2} are logarithms of p and ξ^2 , summing them is equivalent to multiplying p and ξ^2 with the weights as exponents. The weights can be set arbitrarily to emphasize the quality of either light curve fits or fit results. Here, we wish to weight them equally, meaning f_p and f_{ξ^2} should contribute roughly similar values to the overall figure of merit. For the models considered in this analysis, we find that this is roughly satisfied for the simple average of f_p and

f_{ξ^2} , $w_p = w_{\xi^2} = 1$, leaving

$$f \equiv \frac{w_p f_p + w_{\xi^2} f_{\xi^2}}{w_p + w_{\xi^2}} = \frac{f_p + f_{\xi^2}}{2}. \quad (12)$$

We are left with the task of choosing sensible values of p_{\min} and ξ_{\max}^2 such that we do not unnecessarily exclude regions of parameter space, but cut off regions where the fits and population model are not informative. For f_p , we conservatively choose a limit of $p_{\min} = 10^{-4}$ which corresponds to an explosion model lying almost 4σ off our population model. At such low levels of likelihood, our model is not constrained, and the explosion model has been ruled out anyway. For f_{ξ^2} , a limit of $\xi_{\max}^2 = 25$ seems sensible, corresponding to the light curves deviating 5σ from the SALT2 model on average.

We emphasize once again that f should not be assigned any statistical meaning, since f_{ξ^2} has no statistical meaning; f merely serves as a convenient measure of light curve fit quality. Since each set of light curves is fit multiple times with different filter bands and epoch ranges, we average the figures of merit of the individual fits, and denote the averaged quantities $\langle f_{\xi^2} \rangle$, $\langle f_p \rangle$ and $\langle f \rangle$. When error bars on these quantities are given, they refer to the root mean squared (rms) deviation from the mean figure of merit. Note that this procedure does not imply averaging over viewing angles, which for now we treat as individual SNIa events. Where the figures of merit are also averaged over viewing angle, we denote them $\langle\langle f_{\xi^2} \rangle\rangle$, $\langle\langle f_p \rangle\rangle$ and $\langle\langle f \rangle\rangle$.

When discussing the fitted parameters for particular explosion models (or a particular viewing angle of a model), it would be cumbersome to refer to each of the 12 sets of light curve fits individually. Instead, we wish to compute the most likely x_1 , c and M_B for the explosion model. Thus, we define averages over all fits, $\langle x_1 \rangle$, $\langle c \rangle$ and $\langle M_B \rangle$. We note that these quantities are not used to compute figures of merit, but are used for plotting the fit results on the contour plots of the population model. Since fits with a better goodness-of-fit parameter ξ^2 are bound to give more accurate estimates of the fitted parameters, we define the averaged parameters as a weighted average,

$$\langle x_1 \rangle = \sum_i \frac{x_{1,i}}{\xi_i^2} \bigg/ \sum_i \frac{1}{\xi_i^2} \quad (13)$$

where i runs over all 12 fits except those which failed (meaning they have $\xi^2 > \xi_{\max}^2$, or the SNANA fit failed to converge in the first place). $\langle c \rangle$ and $\langle M_B \rangle$ are defined similarly. Furthermore, we compute the rms deviation from the mean parameters separately for values above and below the mean, respectively. The rms deviations are *not* weighted by ξ^2 , and serve as the error bars shown in Section 3. We emphasize that these error bars do not represent 68% intervals of the likelihood of obtaining a certain parameter, or any other quantity which can be interpreted statistically, but merely give an estimate of the dispersion of a fitted parameter between fits. When the error bars are large, the large rms deviation is usually due to one or a few failed fits which return unreasonable results. Since the mean parameters, $\langle x_1 \rangle$, $\langle c \rangle$ and $\langle M_B \rangle$, are weighted by ξ^2 , they are much more reliable in those cases than the error bars indicate. Furthermore, we note that we do not compute fit results averaged over viewing angle (such as $\langle\langle x_1 \rangle\rangle$), but instead plot separate fit results for each viewing angle, giving an impression of the variations of fit results with viewing angle.

3. RESULTS

Table 2
Figures of Merit for All Analyzed Explosion Models

Explosion Model	f^a	σ_θ^b	θ_{\min}	θ_{\max}	σ_{fr}^c	f_{ξ^2}	σ_θ	θ_{\min}	θ_{\max}	σ_{fr}	f_p	σ_θ	θ_{\min}	θ_{\max}	σ_{fr}
KRW09_iso_5_dc_1	0.909	0.009	0.885	0.924	0.078	0.93	0.02	0.88	0.95	0.07	0.89	0.01	0.87	0.90	0.04
KRW09_asym_1_dc_3	0.891	0.031	0.821	0.925	0.100	0.86	0.06	0.73	0.94	0.09	0.92	0.03	0.83	0.96	0.04
KRW09_iso_8_dc_1	0.890	0.029	0.808	0.919	0.119	0.89	0.04	0.80	0.93	0.11	0.89	0.02	0.81	0.93	0.04
KRW09_asym_1_dc_2	0.884	0.029	0.797	0.914	0.106	0.85	0.04	0.74	0.90	0.10	0.92	0.04	0.82	0.97	0.03
KRW09_iso_3_dc_1	0.873	0.014	0.833	0.889	0.105	0.89	0.03	0.82	0.92	0.10	0.86	0.00	0.85	0.86	0.04
KRW09_iso_4_dc_1	0.869	0.029	0.816	0.909	0.103	0.88	0.03	0.81	0.92	0.09	0.86	0.03	0.79	0.90	0.04
KRW09_iso_3_dc_2	0.839	0.022	0.813	0.887	0.087	0.71	0.04	0.66	0.81	0.09	0.97	0.00	0.96	0.97	0.02
KRW09_asym_2_dc_2	0.833	0.023	0.790	0.873	0.080	0.72	0.05	0.64	0.80	0.07	0.95	0.01	0.93	0.97	0.03
KRW09_iso_8_dc_2	0.831	0.040	0.701	0.864	0.087	0.68	0.08	0.44	0.74	0.09	0.99	0.01	0.96	0.99	0.01
KRW09_iso_5_dc_2	0.828	0.015	0.791	0.846	0.064	0.67	0.03	0.59	0.70	0.06	0.99	0.00	0.98	0.99	0.01
KRW09_iso_6_dc_1	0.820	0.034	0.690	0.846	0.127	0.87	0.06	0.61	0.91	0.10	0.77	0.01	0.74	0.79	0.07
KRW09_iso_2_dc_3	0.819	0.055	0.695	0.873	0.130	0.83	0.06	0.69	0.89	0.10	0.81	0.05	0.70	0.86	0.08
KRW09_iso_4_dc_2	0.817	0.024	0.784	0.862	0.087	0.68	0.04	0.62	0.75	0.08	0.96	0.03	0.87	0.99	0.02
KRW09_iso_6_dc_2	0.816	0.055	0.683	0.874	0.117	0.76	0.08	0.57	0.85	0.09	0.87	0.03	0.79	0.91	0.07
KRW09_iso_2_dc_2	0.799	0.036	0.709	0.835	0.137	0.85	0.04	0.76	0.89	0.11	0.75	0.04	0.65	0.78	0.08
KRW09_asym_5_dc_3	0.786	0.026	0.735	0.824	0.140	0.82	0.04	0.74	0.88	0.10	0.75	0.01	0.73	0.77	0.10
KRW09_iso_7_dc_2	0.786	0.019	0.756	0.824	0.063	0.58	0.04	0.52	0.65	0.06	0.99	0.01	0.96	1.00	0.01
KRW09_asym_4_dc_3	0.785	0.017	0.736	0.808	0.127	0.87	0.03	0.76	0.91	0.10	0.70	0.04	0.63	0.78	0.08
KRW09_asym_5_dc_2	0.785	0.018	0.743	0.810	0.138	0.85	0.03	0.79	0.89	0.11	0.72	0.01	0.68	0.74	0.09
KRW09_iso_1_dc_5	0.785	0.016	0.751	0.809	0.166	0.79	0.03	0.73	0.83	0.12	0.78	0.01	0.75	0.79	0.12
KRW09_iso_1_dc_3	0.784	0.010	0.762	0.799	0.150	0.82	0.02	0.78	0.85	0.11	0.75	0.01	0.73	0.76	0.10
KRW09_iso_1_dc_4	0.784	0.010	0.762	0.799	0.150	0.82	0.02	0.78	0.85	0.11	0.75	0.01	0.73	0.76	0.10
KRW09_iso_1_dc_2	0.783	0.007	0.772	0.795	0.147	0.84	0.02	0.81	0.87	0.12	0.72	0.01	0.70	0.74	0.09
KRW09_asym_4_dc_2	0.773	0.021	0.688	0.794	0.138	0.86	0.05	0.73	0.91	0.11	0.68	0.04	0.63	0.76	0.08
KRW09_iso_6_dc_3	0.770	0.047	0.667	0.824	0.104	0.62	0.06	0.47	0.69	0.08	0.92	0.03	0.87	0.96	0.06
KRW09_iso_2_dc_5	0.764	0.045	0.664	0.813	0.102	0.63	0.05	0.50	0.69	0.08	0.90	0.04	0.77	0.94	0.06
KRW09_asym_3_dc_3	0.764	0.022	0.716	0.789	0.132	0.83	0.03	0.72	0.86	0.12	0.69	0.04	0.61	0.75	0.06
KRW09_asym_2_dc_3	0.757	0.021	0.722	0.806	0.064	0.53	0.04	0.45	0.62	0.06	0.99	0.00	0.98	1.00	0.01
KRW09_asym_3_dc_2	0.750	0.018	0.703	0.769	0.139	0.82	0.02	0.76	0.85	0.12	0.68	0.04	0.60	0.73	0.06
KRW09_iso_3_dc_3	0.747	0.028	0.715	0.803	0.052	0.50	0.05	0.45	0.61	0.05	0.99	0.00	0.98	1.00	0.01
KRW09_iso_8_dc_3	0.743	0.029	0.670	0.770	0.083	0.52	0.06	0.37	0.58	0.08	0.96	0.01	0.92	0.98	0.02
KRW09_asym_7_dc_3	0.729	0.027	0.632	0.759	0.160	0.81	0.04	0.65	0.84	0.14	0.65	0.02	0.59	0.68	0.08
KRW09_iso_6_dc_4	0.725	0.034	0.651	0.764	0.098	0.50	0.05	0.36	0.55	0.09	0.95	0.02	0.90	0.98	0.04
KRW09_iso_4_dc_3	0.718	0.021	0.687	0.756	0.077	0.47	0.05	0.41	0.58	0.07	0.97	0.02	0.87	0.98	0.02
KRW09_asym_7_dc_2	0.715	0.040	0.544	0.745	0.175	0.80	0.06	0.57	0.84	0.16	0.63	0.03	0.52	0.66	0.08
KRW09_iso_7_dc_3	0.710	0.028	0.670	0.775	0.073	0.47	0.04	0.40	0.57	0.06	0.95	0.02	0.93	0.98	0.03
KRW09_iso_6_dc_5	0.710	0.031	0.646	0.746	0.091	0.45	0.05	0.32	0.51	0.09	0.97	0.02	0.93	0.99	0.03
W7	0.700				0.146	0.60				0.09	0.80				0.12
KRW09_asym_8_dc_3	0.692	0.021	0.643	0.717	0.172	0.79	0.02	0.74	0.83	0.15	0.59	0.04	0.52	0.65	0.09
KRW09_iso_4_dc_4	0.690	0.031	0.654	0.747	0.090	0.44	0.07	0.38	0.63	0.08	0.94	0.03	0.84	0.96	0.04
KRW09_asym_6_dc_3	0.686	0.028	0.621	0.715	0.182	0.77	0.05	0.61	0.81	0.16	0.60	0.03	0.54	0.63	0.08
PreExp60	0.685	0.055	0.604	0.821	0.403	0.63	0.10	0.41	0.82	0.32	0.74	0.11	0.57	0.91	0.23
KRW09_iso_5_dc_3	0.676	0.026	0.622	0.705	0.064	0.41	0.04	0.34	0.45	0.05	0.94	0.02	0.91	0.96	0.04
KRW09_asym_6_dc_2	0.676	0.021	0.620	0.700	0.184	0.77	0.03	0.69	0.80	0.16	0.58	0.03	0.49	0.61	0.09
KRW09_asym_8_dc_2	0.668	0.016	0.629	0.688	0.187	0.79	0.03	0.72	0.82	0.15	0.55	0.04	0.47	0.61	0.11
KRW09_iso_5_dc_4	0.642	0.027	0.586	0.668	0.090	0.41	0.04	0.34	0.46	0.06	0.87	0.02	0.83	0.89	0.06
PreExp30	0.571	0.092	0.285	0.655	0.222	0.54	0.11	0.23	0.65	0.20	0.60	0.08	0.34	0.66	0.09
PreExp80	0.380	0.101	0.251	0.569	0.333	0.55	0.07	0.46	0.73	0.31	0.21	0.17	0.00	0.53	0.08
PureDef_0128_256	0.331				0.042	0.02				0.04	0.64				0.01
PureDef_0150_128	0.316				0.187	0.12				0.12	0.51				0.14
PureDef_0063_128	0.302				0.174	0.05				0.07	0.56				0.16
PureDef_1700_384	0.142				0.338	0.28				0.34	0.00				0.00
PureDef_1100_256	0.142				0.347	0.28				0.35	0.00				0.00
PureDef_3500_384	0.124				0.299	0.25				0.30	0.00				0.00

Note. — The models in this table are sorted by a descending overall figure of merit, $\langle\langle f \rangle\rangle$. Some of the column headers take on slightly different meanings compared to the text, as explained in the comments below. The original KRW09 paper lists 44 models, but accidentally no radiative transfer results were computed for iso_1_dc_4 (Blondin et al. 2011). See Section 3 for a discussion of these results.

^a The bold columns f , f_{ξ^2} and f_p refer to the viewing angle averaged figures of merit, $\langle\langle f \rangle\rangle$, $\langle\langle f_{\xi^2} \rangle\rangle$ and $\langle\langle f_p \rangle\rangle$, where multiple viewing angles were present. Otherwise, they refer to the figures of merit averaged over fits, $\langle f \rangle$, $\langle f_{\xi^2} \rangle$ and $\langle f_p \rangle$.

^b The three columns to the right of each figure of merit show the standard deviation in viewing angle, σ_θ , as well as the minimum and maximum figure of merit in any one viewing angle, denoted θ_{\min} and θ_{\max} . For models with only one viewing angle, these columns are blank.

^c The fourth column to the right of each figure of merit shows the standard deviation over the 12 fits performed, σ_{fr} . For models with multiple viewing angles, σ_{fr} is the average of the standard deviations in each viewing angle. Due to failed fit runs, the overall figure of merit can only be computed for the average of all fits, i.e. $\langle f \rangle$, and the standard deviation of $\langle f \rangle$ is the quadratic sum of the standard deviations on $\langle f_p \rangle$ and $\langle f_{\xi^2} \rangle$. Generally, the standard deviation of the figures of merit over the 12 fits, σ_{fr} , is large which is expected, particularly for models which exhibit poor light curve fits (see Section 2.3).

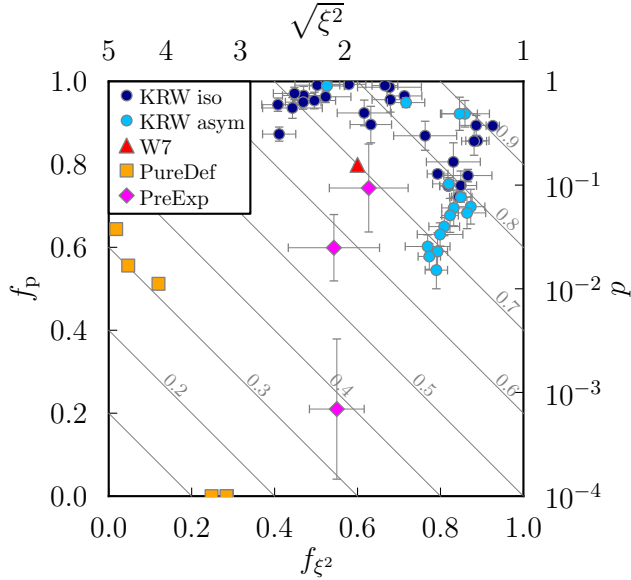


Figure 6. The figures of merit from Table 2, with the quality of the light curve fit, $\langle\langle f_{\xi^2} \rangle\rangle$, increasing to the right, and the likelihood to observe a SNIa with the fitted parameters in nature, $\langle\langle f_p \rangle\rangle$, increasing toward the top. The diagonal gray lines and labels show lines of constant overall figure of merit. The error bars show the dispersion of the figures of merit between the viewing angles of a given model. The top axis indicates how many standard deviations the model light curves deviate from the SALT2 model on average as a function of f_{ξ^2} , while the right axis shows the p -values corresponding to f_p .

With the machinery developed in the previous section, we are now in a position to compute figures of merit in a fully automated way. Table 2 lists the figures of merit for goodness-of-fit, fitted parameters, and the overall figure of merit for all explosion models introduced in Section 2.1. Figure 6 shows the distribution of $\langle\langle f_{\xi^2} \rangle\rangle$ and $\langle\langle f_p \rangle\rangle$ graphically. The overall figures of merit span a range of $0.124 \leq \langle\langle f \rangle\rangle \leq 0.909$, most of the allowed range of $0 < \langle\langle f \rangle\rangle < 1$. The figure of merit for fitted parameters, $\langle\langle f_p \rangle\rangle$, spans almost the entire possible range, $0 \leq \langle\langle f_p \rangle\rangle \leq 0.99$, meaning that the explosion models lie both at the very center of the population and entirely outside it. The figure of merit for light curve fit, $\langle\langle f_{\xi^2} \rangle\rangle$, exhibits only a slightly smaller range with $0.02 \leq \langle\langle f_{\xi^2} \rangle\rangle \leq 0.93$. In the following sections we discuss the results for each family of explosion models.

3.1. The KRW09 Delayed-detonation Models

Generally, all KRW09 models do relatively well ($0.642 \leq \langle\langle f \rangle\rangle \leq 0.909$), particularly in matching the population model ($0.55 \leq \langle\langle f_{\xi^2} \rangle\rangle \leq 0.99$). With 43 models in the KRW09 set, a total of 1290 viewing angles and 15,480 fits, it is difficult to give a visual impression of the various light curves and fits. Figure 7 shows three selected light curve fits for some of the highest and lowest ranked viewing angles. In order to give an overview of the region of SALT2 parameter space occupied by the KRW09 models, the top row of Figure 8 shows the location of all KRW09 models on the parameter space plots. For clarity, the error bars are omitted. On average, the asymmetric models tend to be slightly brighter and redder than the isotropic models. The isotropic models lie somewhat closer to the center of the population distribution in all three panels. This trend is reflected in the higher $\langle\langle f_p \rangle\rangle$ that the isotropic models receive on average (Figure 6). We emphasize that this observation refers only to the isotropic and asymmetric cases investigated by KRW09, and is not a statement about isotropic

or asymmetric models in general.

The bottom row of Figure 8 shows the locations of a few selected models, including those with the highest and lowest $\langle\langle f \rangle\rangle$, and highest and lowest $\langle\langle f_p \rangle\rangle$. While the error bars on the color parameter can be quite large, we note that the error bars represent the standard deviation given the set of 12 fits performed, and are usually dominated by one or a few poor fits. Since the average values plotted are *weighted* averages, the fitted parameters from the bad fit runs are essentially ignored, and the average value is presumably more reliable than the error bars indicate (see discussion in Section 2.5).

One might suspect that the asymmetric models would exhibit systematically different light curves with viewing angle, and thus a larger dependence of their figure of merit with viewing angle. Such a trend, however, is not apparent in the dispersions of $\langle f \rangle$ with viewing angle (σ_θ in Table 2), or in the parameter space plots in Figure 8. In fact, the two models with the highest dispersion are iso_2.dc_3 and iso_6.dc_2 ($\sigma_\theta = 0.055$), though a low dispersion in the figure of merit does not automatically mean that the fitted parameters show a low dispersion as well.

The asymmetric models show a few interesting trends (light blue points in Figure 6). First, the asym_1 models (dc 2 and 3) both receive excellent figures of merit, and lie in the top right corner of the plot. The asym_2 models have slightly brighter magnitudes, but receive equally excellent $\langle\langle f_p \rangle\rangle$. Their light curve fit, however, is degraded by a shallower rising slope, moving them to the top center of the plot. All other asym models share roughly the same $\langle\langle f_{\xi^2} \rangle\rangle \approx 0.8$ because their light curves exhibit very similar shapes. Their magnitudes, however, become brighter, roughly in the order asym_5, 4, 3, 7, 6 and 8, moving them away from the center of the population model, with the dc_3 versions performing slightly better than their dc_2 counterparts. Overall, it appears that those models with more ignition bubbles (asym_1 and 2) perform better than those with fewer bubbles. More bubbles mean a stronger deflagration, and thus a less powerful detonation and a dimmer peak magnitude, in better agreement with the population model. For the isotropic models, the comparable trends are much less clear (dark blue points in Figure 6).

The KRW09 models have been compared with observations before, namely in the original KRW09 paper and in Blondin et al. (2011). Figure 3 of KRW09 demonstrates that the models broadly follow the Phillips relation, with only a few models outside the 1σ contour. Furthermore, the models adhere to the observed color–magnitude relation, with some scatter. We confirm both results, though some models lie outside our 2σ contours because their peak magnitudes range toward the bright end of the observed distribution.

Blondin et al. (2011) excluded six of the models on the basis of spectral comparisons, namely the dc_2 and dc_3 versions of asym_3, asym_6 and asym_8. The asym_6 and asym_8 models are the lowest ranked asymmetric models according to our method ($0.668 \leq \langle\langle f \rangle\rangle \leq 0.692$), while the asym_3 models range in mid-field ($0.75 \leq \langle\langle f \rangle\rangle \leq 0.764$), meaning that none of these models are excluded in our analysis. Out of a subset of eight models which were analyzed in detail in Blondin et al. (2011), iso_3.dc_1 and asym_1.dc_3 showed the best and third-best spectral matches with observations. These model are among the highest ranked models in our analysis as well ($\langle\langle f \rangle\rangle = 0.873$ and 0.891 , respectively). On the other hand, the second-best spectral match, iso_6.dc_5, ranges toward the bottom of the table in our analysis ($\langle\langle f \rangle\rangle = 0.710$). Such discrepancies highlight that a good spectral match and good light

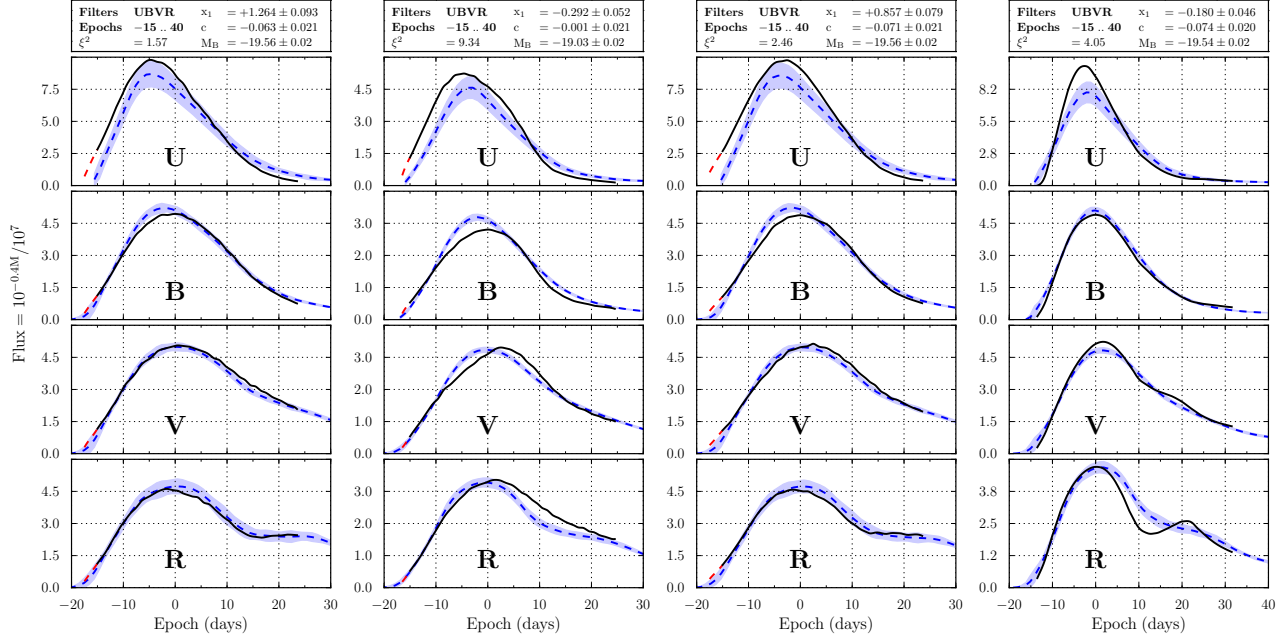


Figure 7. *UBVR* light curve fits to three KRW09 models (left three columns) and W7 (right column), including all epochs from -15 to $+40$ days. The lines have the same meaning as in Figure 2. Left column: the 51° viewing angle of the *iso_5_dc_1* model, the viewing angle with the highest $\langle f_{\ell^2} \rangle = 0.95$. Second column: the 165° viewing angle of the *iso_6_dc_5* model, the viewing angle with the lowest $\langle f_{\ell^2} \rangle = 0.32$. Third column: the 88° viewing angle of the *iso_6_dc_2* model which we will analyze in detail in Section 4.2. Right column: the W7 model is well fit with SALT2 across the entire epoch range, particularly in the *B* and *V* bands ($\langle \langle f \rangle \rangle = 0.700$).

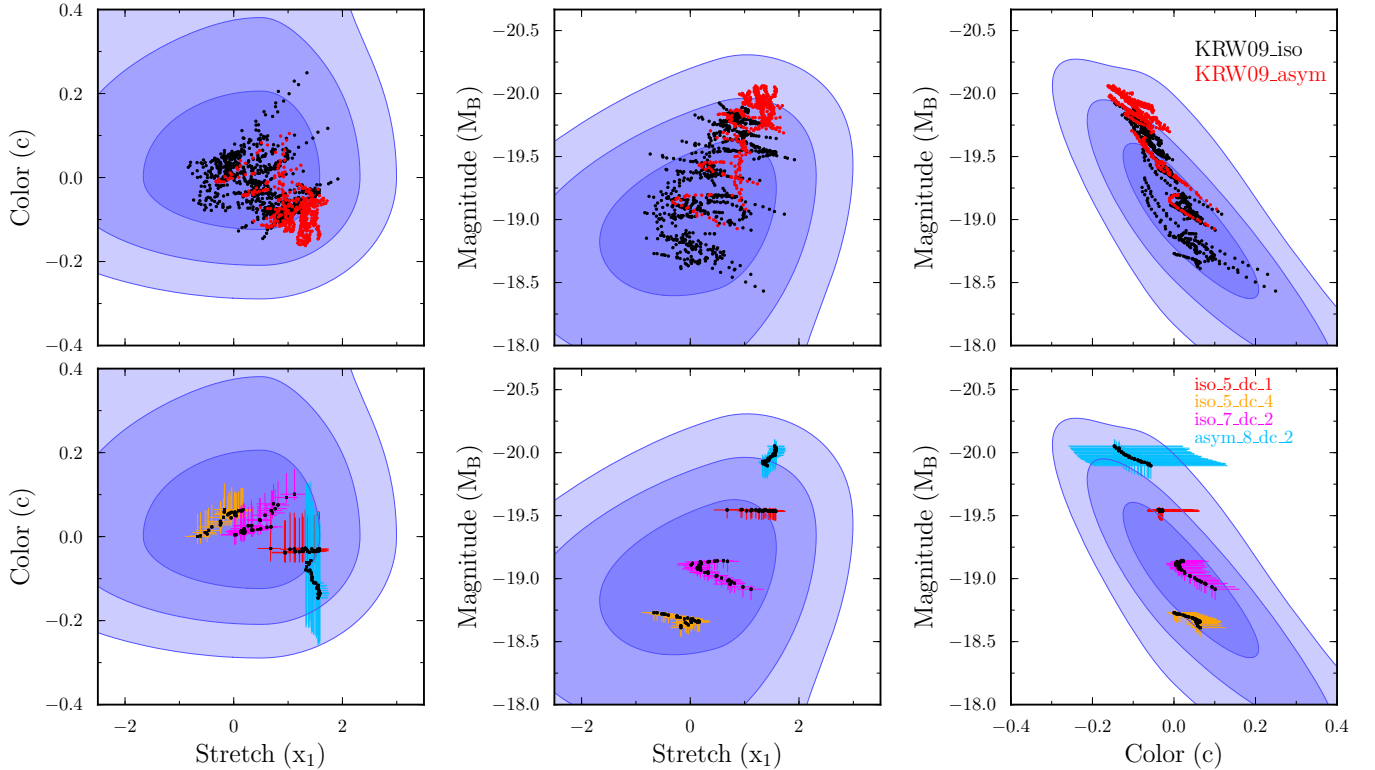


Figure 8. Fit results for the KRW09 models. Top row: Fit results for all viewing angles of all KRW09 models, plotted without error bars for clarity. The KRW09 models occupy a favorable region of parameter space, with a few models outside the 2σ contours in the stretch–magnitude and color–magnitude planes. On average, the isotropic models (black) are slightly favored over the asymmetric models (red). Bottom row: Fit results for several individual models including *iso_5_dc_1* (red, highest $\langle \langle f \rangle \rangle$), *iso_5_dc_4* (orange, lowest $\langle \langle f \rangle \rangle$), *iso_7_dc_2* (pink, highest $\langle \langle f_p \rangle \rangle$), and *asym_8_dc_2* (cyan, lowest $\langle \langle f_p \rangle \rangle$). Even the farthest outlying viewing angle of *asym_8_dc_2* is not excluded by the population model (see the light curve fit for this viewing angle in Figure 7).

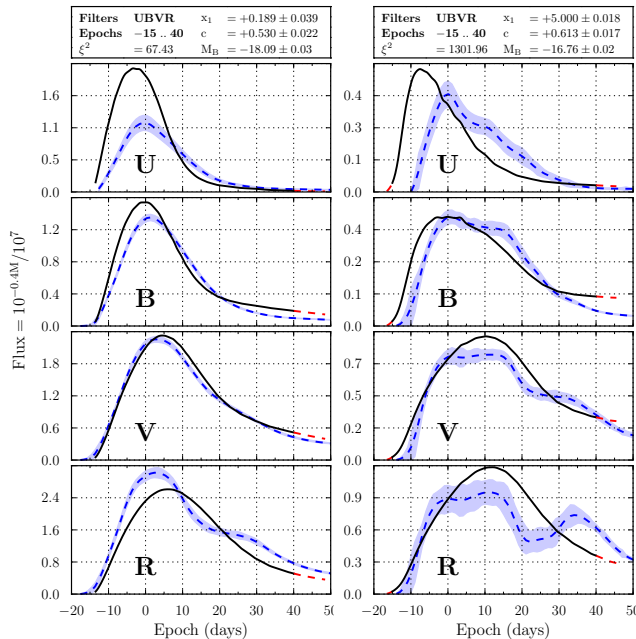


Figure 9. *UBVR* light curve fits to the PureDef_0128_256 (left column) and PureDef_3500_384 (right column) models. The lines have the same meaning as in Figure 2. PureDef_0128_256 receives the best overall figure of merit of all PureDef models, PureDef_3500_384 the worst. See Section 3.3 for a discussion of the large uncertainties on the SALT2 model in the PureDef_3500_384 fit.

curve fit are not necessarily correlated. When spectra are integrated over broad-band filters in order to generate magnitudes, discrepant features which might degrade a spectral comparison are washed out in favor of the overall normalization, which is in turn ignored in most spectral comparisons. The resulting differences between spectral and light curve comparisons were highlighted, for example, in Figure 7 of Blondin et al. (2011) which demonstrates that those KRW09 models with good spectral matches are only slightly more likely to match the Phillips relation.

3.2. The W7 Model

As expected from the discussion in Section 2.1, Table 2 shows that W7 agrees with observed light curves quite well. The average figures of merit for the light curve fits are $\langle f_{\xi^2} \rangle = 0.60$, $\langle f_p \rangle = 0.80$ and $\langle f \rangle = 0.700$, as shown by the red triangle in Figure 6. The right column of Figure 7 shows *UBVR* light curve fits to the W7 model, fit over the entire epoch range computed by Phoenix. The goodness-of-fit parameter ξ^2 suffers mainly from two features of the light curves, namely the high *U*-band peak brightness and the strong second peak in *R*-band.

The fitted parameters for W7 match observations as well as the light curves, as shown with the black data points in Figure 10. W7 also lies well within the range of the population model, though slightly on the bright side for its stretch and color. Since W7 is not a very physical model (see Section 2.1), there are no deep insights to be taken away from these results. They simply demonstrate that our method arrives at the accepted conclusion that W7 represents observed light curves surprisingly well.

3.3. Pure Deflagration Models

Though underluminous SNeIa have recently received increased attention (Foley et al. 2013), they constitute at best a

sub-class of SNeIa. They are not well represented in observed samples because they are both less frequent and dim, and thus hard to detect. Pure deflagration models are generally known to result in underluminous SNeIa and may afford an explanation of these events. However, we expect pure deflagration models to receive relatively low figures of merit for two reasons: first, the SALT2 model was trained on normal SNeIa and typically does not fit peculiar Ia well; and secondly, only a small fraction of the SNeIa observed in nature are underluminous, and the population model does not favor them as a result. We return to this issue in Section 5. Once again, we emphasize that the six pure deflagration models investigated here are not necessarily characteristic of pure deflagration models in general, as they represent a small subset of the possible ignition configurations and other parameters.

Figure 6 demonstrates that the pure deflagration models, shown with orange squares, separate into two groups: those with few ignition points (63, 128 and 150, $0.302 \leq \langle f \rangle \leq 0.331$) and those with many (1100, 1700 and 3500, $0.124 \leq \langle f \rangle \leq 0.142$). The few-bubble models occupy an untypical location in $\langle f_{\xi^2} \rangle$ - $\langle f_p \rangle$ space, as they combine poor light curve fits with favorable fitted parameters.

The left column of Figure 9 shows light curve fits to the few-bubble model PureDef_0128_256. The fit is extremely poor in *U*-band, and thus receives a low figure of merit, as do the other few-bubble models ($0.05 \leq \langle f_{\xi^2} \rangle \leq 0.12$). The fitted parameters shown in Figure 10, however, reveal a different picture. The few-bubble models (red, cyan and blue data points) can be accommodated by the population model, with figures of merit of $0.51 \leq \langle f_p \rangle \leq 0.64$. We note that the few-bubble models exhibit very small error bars on stretch and magnitude, despite their mediocre light curve fits. As discussed in Section 2.3, poor fits are generally more sensitive to changes in filter bands and epoch range, and we might thus expect large uncertainties on the PureDef models. In this case, however, the discrepancy with the SALT2 model is largely driven by the excessive *U*-band flux of the few-bubble models. When only the *B* and *V* bands are fit, the fitted color is much redder than that of the full *UBVR* fit. As a result, the uncertainty in the fitted color parameter is significantly larger than the uncertainty in stretch and magnitude.

In contrast to the few-bubble models, the many-bubble models (purple, yellow and green data points in Figure 10) are clearly excluded by the population model ($\langle f_p \rangle = 0$). Their light curve fits, however, receive slightly higher figures of merit ($0.25 \leq \langle f_{\xi^2} \rangle \leq 0.28$), seemingly in conflict with the poor light curve fit to the many-bubble model PureDef_3500_384 (right column of Figure 9). While the particular fit shown receives $f_{\xi^2} = 0$ due to the large *U*-band discrepancy with the SALT2 model, the *BV* bands can be fit reasonably well, and the model receives a goodness-of-fit score of $\langle f_{\xi^2} \rangle = 0.25$. The reason for this comparatively high score is that the uncertainties on the SALT2 model light curves are much larger than for the fits to other models. SALT2 assigns these increased uncertainties whenever the fit is driven to an extreme region of parameter space, in this case large stretch, red color and dim magnitude. Since very few such events have been observed in nature, the SALT2 flux surfaces are poorly constrained which is reflected in the larger uncertainties. At first sight, the larger uncertainties seem to pose a problem since they cause $\langle f_{\xi^2} \rangle$ to reward fits with extreme parameters. However, extreme fitted parameters automatically mean a very small likelihood of observing a comparable SNIa in nature, and thus a very low $\langle f_p \rangle$. Indeed, $\langle f_p \rangle = 0$ for the

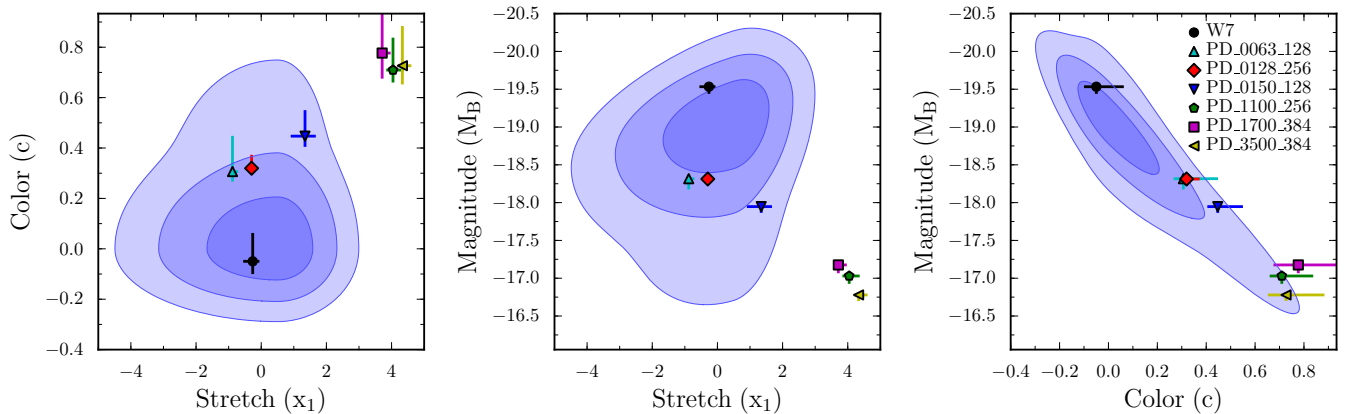


Figure 10. Fit results for the W7 and pure deflagration models. The W7 model (black data point) is known to reproduce observed light curves well which is confirmed here, though W7 lies toward the bright end of the stretch–magnitude and color–magnitude relations. The pure deflagration models split into two groups, those with a few ignition bubbles (PureDef_0128_256, PureDef_0150_128 and PureDef_0063_128; red, cyan and blue data points) which are not in the center of the distribution, but certainly not ruled out either, and three models with many ignition bubbles. The latter are clearly ruled out by the population model as the values of both their stretch and color are higher than observed SNeIa.

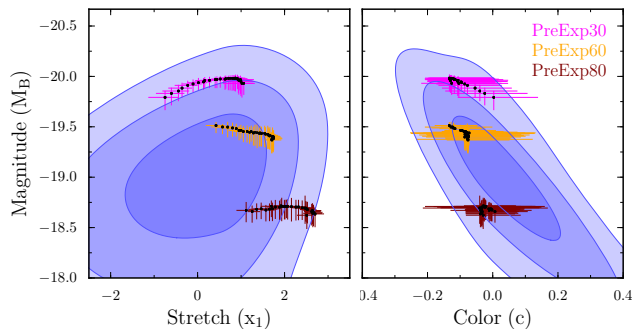


Figure 11. Fit results for the three pre-expanded models. Almost all viewing angles lie within the allowed region of color–stretch space (not shown). The PreExp80 model exhibits the largest scatter of $\langle f \rangle$ with viewing angle of any model. The amount of pre-expansion (30%, 60% and 80% of the binding energy, respectively) appears to mostly change the peak magnitude of the light curves, but not the decline rate. As a consequence, the three models lie on a trajectory perpendicular to the Phillips relation.

PureDef_3500_384 model, meaning that the model is deemed incompatible with observations despite its “unfairly” reasonable $\langle f_{e^2} \rangle$. Since we are not particularly interested in the exact numerical values of $\langle f \rangle$ for poorly fitting models, the imbalance in $\langle f_{e^2} \rangle$ does not lead to false conclusions.

Overall, our analysis has revealed an interesting distinction between models with few and many bubbles. At least for this particular set of pure deflagration models, realizations with too many ignition bubbles are ruled out by the population model. Those with few bubbles cannot be accommodated by the SALT2 model, but since SALT2 was not trained on peculiar SNeIa, the PureDef light curves need to be compared to peculiar events directly (M. Long et al. 2013, in preparation).

3.4. Pre-expanded Models

Since the pre-expansion of the white dwarf was varied over a large range (30% to 80% of the binding energy), we expect the pre-expanded models to give diverse results. The fitted parameters shown in Figure 11 confirm this expectation. The PreExp30 and PreExp60 models can be accommodated by the population model, though some viewing angles lie beyond the 2σ contours of the stretch–magnitude and color–magnitude planes ($0.6 \leq \langle \langle f_p \rangle \rangle \leq 0.74$). Some viewing angles of the third model, PreExp80, lie outside the 3σ contours, causing a poor figure of merit for the model overall ($\langle \langle f_p \rangle \rangle = 0.21$).

The amount of pre-expansion appears to mostly change the peak magnitude (since it determines how much material is burned to ^{56}Ni), but not the decline rate. Thus, the models end up on a trajectory perpendicular to the Phillips relation. Since the detonation was initiated significantly off-center, we expect the pre-expanded models to exhibit strong variations with viewing angle. Indeed, the PreExp80 model shows the strongest variations in f between viewing angles of any model ($\sigma_\theta = 0.1$).

Overall, the analysis shows that the PreExp60 model matches observed light curves surprisingly well, considering that it is a very simple, parametric, pure detonation model. This agreement is very sensitive to the amount of pre-expansion though, as brighter or dimmer peak magnitudes move the models away from the Phillips relation. Thus, it is unclear whether such simple pre-expanded models can fill in the rest of the parameter space in color and stretch. The results allow us to constrain which combinations of pre-expansion, contraction and detonation criteria result in a reasonable amount of ^{56}Ni , and thus reasonable magnitudes.

4. DISCUSSION

We have introduced a new method for evaluating simulated SNIa light curves with observations, and applied it to a range of explosion models. In this section we address some remaining questions. In Section 4.1 we discuss the parameter choices we made in designing the population model, and the reliability of those choices. In Section 4.2 we investigate an apparent contradiction between our evaluation method and visual light curve comparisons for one particular explosion model, and discuss potential issues with visual comparisons in general.

4.1. Uncertainties in the Population Model

In this section, we discuss the various uncertainties which may affect our population model, namely the reliability of the global SALT2 parameters, the potential effects of host galaxy extinction, as well as trends with redshift and host galaxy type.

4.1.1. The Global SALT2 Parameters

The population model parameters listed in Table 1 were determined by comparing data and Monte-Carlo simulations in

Table 3
Values for the Global SALT2 Parameters from the Literature

Reference	Data Set	Model	α	β	M_0	H_0	σ_{int}
Sullivan et al. (2011) ^a	SNLS	SiFTO	0.132 – 0.138	3.17 – 3.25			
Conley et al. (2011) ^a	SNLS, SDSS, low- z , <i>HST</i>	SiFTO	0.132 – 0.138	3.17 – 3.25			0.068 – 0.113
Guy et al. (2010) ^a	SNLS	SALT2/ SiFTO	0.124 ± 0.012	3.17 ± 0.13	-19.095 ± 0.032 [†]	70	0.087
Marriner et al. (2011)	SDSS (four seasons)	SALT2	$0.135^{+0.033}_{-0.017}$	$3.19^{+0.14}_{-0.24}$			
Campbell et al. (2013)	SDSS (all seasons)	SALT2	0.22 ± 0.02	3.12 ± 0.12			

Note. — The model column refers to the fit model for which values are given in the reference, even though other fit models may also have been used for the analysis. Wherever a range of parameters is given, different fits were performed, and the differences between their results were greater than the statistical error quoted.

^a The parameters from the recent SNLS3 analyses were re-scaled from SiFTO. Since SiFTO uses slightly different color and stretch corrections, α , β and the uncorrected magnitude M_0 also take on slightly different meanings. Linear re-scaling formulae for α and β are given in G10. In their paper, the SiFTO M_0 is given as $M_0 = 19.218 \pm 0.032$ and was re-scaled to the value above (Guy 2012, private communication).

K13, and from examining the extreme tails of the nearby sample. The global SALT2 parameters α , β , M_0 and σ_M , however, are derived from a Hubble diagram fit, with fits to different data sets resulting in somewhat different values of the parameters (Table 3). Such discrepancies arise either because surveys are biased, or because the true, underlying parameters are redshift-dependent, and different surveys probe different redshift ranges. Table 3 only lists analyses which used the G10 version of the SALT2 model or the SiFTO model, where SiFTO parameters were re-scaled to the corresponding SALT2 values (G10).

For the population model, we rely on the results of the most recent SNLS3 analyses, $\alpha = 0.13$, $\beta = 3.2$ and $M_0 = -19.095$ (G10; Sullivan et al. 2011; Conley et al. 2011). These SNLS3 results, however, are in tension with the most recent analysis of SDSS data (Campbell et al. 2013) who find an unusually high value of $\alpha = 0.22 \pm 0.02$ in their photometric sample, 4.5σ off the SNLS3 value. However, they suspect that the discrepancy may be due to non-Ia contamination, and find a lower value of $\alpha = 0.16 \pm 0.02$ when only fitting spectroscopically confirmed events.

In order to quantify the impact of the uncertainties on α and β , we plot confidence contours of the population model for values which differ from the fiducial values by 2σ , using the uncertainties from G10. The top two panels of Figure 12 show stretch–magnitude and color–magnitude contours for our fiducial population model ($\alpha = 0.13$ and $\beta = 3.2$), as well as contours for $\alpha = 0.106$ and $\alpha = 0.154$. The contours are barely distinguishable from the fiducial model. In the bottom panels of Figure 12 we show the same plots, with $\beta = 2.94$ and $\beta = 3.46$. The differences to the contours of the fiducial model are marginally larger than when varying α , but still small, particularly for the 68% and 95% contours. In conclusion, we find that our values for α and β reflect the most recent observational data, and that our population model is barely sensitive to their uncertainties.

While the choice of α and β does not have a significant impact on our population model, the choice of M_0 clearly does. Its impact would manifest itself in Figure 12 by shifting the contours up and down in magnitude, while the explosion model M_B would stay the same. As the scatter in SNIa magnitudes is only $\sigma_M = 0.13$, fractions of a magnitude matter. We note that, in the context of the SALT2 model, M_0 is the uncorrected ($x_1 = c = 0$) absolute B -band magnitude of SNeIa, *not* their average magnitude. While the magnitude distribution of SNeIa has been quantified (Yasuda & Fukugita 2010; Li et al. 2011b), M_0 must be derived from a Hubble diagram

fit to SALT2 fitted SNeIa. Unfortunately, M_0 is often ignored in cosmological analyses since it is degenerate with H_0 and can be scaled out without influencing cosmological results.

As with α and β , we choose the value of M_0 found in the most recent SNLS 3-year analysis of G10. It is crucial to note that this choice of M_0 corresponds to their assumed Hubble constant, $H_0 = 70 \text{ km s}^{-1} \text{ Mpc}^{-1}$ (G10). The exact value of H_0 has recently been subject to debate; while the final *WMAP9* analysis of Hinshaw et al. (2012) found $H_0 = 69.3 \pm 0.8$, the newer Planck data favor a lower value of 67.80 ± 0.77 (Planck Collaboration et al. 2013). In general, the values inferred from cosmic microwave background analyses are in tension with local universe measurements (e.g., 73.8 ± 2.4 from Cepheid variables, Riess et al. 2011). In light of such large systematic differences, we conclude that our value of $H_0 = 70 \text{ km s}^{-1} \text{ Mpc}^{-1}$ represents a reasonable compromise between the current measurements. We do, however, caution that significant shifts in the best estimate of H_0 could change M_0 noticeably, namely by 0.03 magnitudes for each $1 \text{ km s}^{-1} \text{ Mpc}^{-1}$ change in H_0 . For example, if the Planck value of 67.8 turned out to be correct, M_0 would shift by 0.07 magnitudes. This implicit uncertainty in M_0 should be seen as part of our standard deviation in magnitude, σ_M .

Table 3 shows that different analyses arrive at different conclusions regarding the intrinsic scatter in magnitude, σ_M , which is an important input parameter to our population model since it directly determines the model’s tolerance for magnitudes offset from the mean magnitude–stretch and magnitude–color relations. Our value for the intrinsic scatter in magnitude, $\sigma_M = 0.13$, represents the coherent scatter model of K13. They found that this model (a wavelength-independent scatter of 0.13 magnitudes) reproduces the scatter observed in the Hubble diagram fit to SDSS and SNLS data.

4.1.2. Host Galaxy Extinction

Host galaxy extinction could affect our population model in two separate ways. First, the color distribution derived in K13 includes the intrinsic population convolved with host galaxy extinction, meaning that the true, underlying distribution might contain more blue SNeIa than our population model implies. Secondly, the model assumes that the color–magnitude relation in SNeIa is intrinsic, and should thus be obeyed by explosion models. Let us discuss these aspects in turn.

Constraining the amount of dust extinction in SNeIa has been a long-standing challenge (Riess et al. 1996a,b), par-

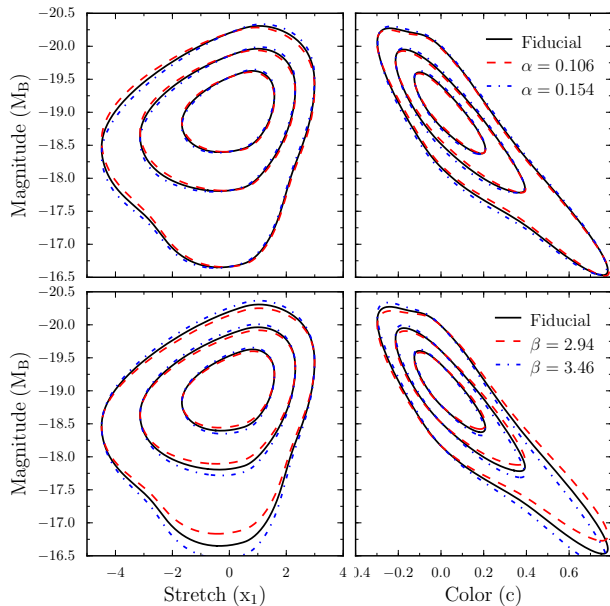


Figure 12. Sensitivity of the population model to changes in α and β . Each row shows stretch–magnitude and color–magnitude contours for the fiducial population model ($\alpha = 0.13, \beta = 3.2$), as well as contours with $\alpha \pm 2\sigma_\alpha$ (top panels) and $\beta \pm 2\sigma_\beta$ (bottom panels), using the uncertainties from G10. The population model is remarkably stable against those changes in α and β .

tially because the extinction law parameter, R_V , and thus the amount of color variation, is difficult to constrain (Jha et al. 2007). Nevertheless, we attempt a simple estimate of the impact of extinction on the color distribution. We use the extinction distribution of Wood-Vasey et al. (2007) which is based on theoretical work by Hatano et al. (1998) and Riello & Patat (2005), as well as a fiducial value of $R_V = 3.1$, and compute the shift in the underlying color distribution which reproduces the observed distribution when convolved with the extinction distribution. We find that the center of the distribution remains at 0, but that virtually all SNeIa with $c > 0.2$ are accounted for by extinction, not intrinsic color variations. This result implies that either (1) there are no intrinsically red SNeIa or (2) the assumed distribution overestimates the amount of extinction significantly.

Given these fundamental uncertainties, we choose to remain agnostic and ignore host galaxy extinction in our population model. We did, however, compute all figures of merit based on the extinction-corrected population model described above. The average $\langle\langle f_p \rangle\rangle$ of all models is lowered only slightly, from 0.701 to 0.689. The KRW09 models are barely affected since they lie towards the blue end of the color distribution. Those models with red colors, however, are strongly affected by the correction. For example, the average $\langle f_p \rangle$ of the few-bubble pure deflagration models drops from 0.57 to 0.

Besides the uncertainty in the underlying color distribution, extinction changes the interpretation of the nature of color variations in SNeIa. When using the population model to evaluate simulated SNeIa light curves, we assume that the color–magnitude relation is intrinsic, and should thus be obeyed by explosion models. If, however, this relation was caused by processes other than the SNIa explosion itself, such as dust extinction, explosion models should show discrepancies, such as never producing highly reddened events. The assumption of an intrinsic color–magnitude relation can only render our model too lenient toward explosion models. Con-

sider the extreme case of a color–magnitude relation which is entirely caused by dust reddening; in that case, explosion models should occupy one particular locus in color–magnitude space which would still be allowed by the population model (the locus of unreddened SNeIa). However, the model would also allow a range of other values of color and magnitude which correspond to the relation imposed by dust reddening. This extreme scenario has been ruled out, for example by Maeda et al. (2011) who investigated a sample of SNeIa which were deemed to be essentially free of host reddening, and found strong evidence for an intrinsic color–magnitude relation. Nevertheless, one should keep this caveat in mind when constraining explosion models using the color–magnitude relation.

4.1.3. Dependence on Redshift and Host Galaxy Type

We note various systematic trends with redshift and host galaxy type which might affect the accuracy of our population model. For example, Conley et al. (2011) found a mild redshift dependence in the best-fit values for α and β . Similarly, it is unclear how exactly the stretch and color populations of SNeIa depend on host galaxy, and thus redshift (Sullivan et al. 2006; Lampeitl et al. 2010; Sullivan et al. 2010; Kelly et al. 2010; Smith et al. 2012). The observed evolution of x_1 and c with redshift can mainly be ascribed to Malmquist bias, but even after accounting for this type of bias the population model parameters from SDSS and SNLS are somewhat inconsistent, with SNLS producing more bright, blue explosions (K13). This disagreement is qualitatively explained by the observation that young, star-forming galaxies tend to produce brighter and bluer SNe (Sullivan et al. 2006). Nevertheless, the best-fit parent populations in color and stretch are slightly different for SDSS and SNLS.

4.1.4. Comparison with the Observed Magnitude Distribution

The distribution of M_B in the population model is derived from the color and stretch distributions, the SALT2 prescription for the correlations between color, stretch, and magnitude (Equation (5)), as well as the chosen values of α , β and M_0 . Thus, comparing the M_B distribution with observed samples is an independent test of the accuracy of the population model.

We compared the distribution of peak magnitudes from our population model with the observed distribution of Li et al. (2011b), a sample of 74 very nearby SNeIa from the Lick Observatory Supernova Search (LOSS, Leaman et al. 2011). The distributions generally agree, but the LOSS sample shows an excess at dim magnitudes. The sample was taken at $z \approx 0$ (at a maximum distance of 80 Mpc), whereas the population model is trained on SDSS and SNLS data sets whose mean redshift is larger. Thus, the discrepancy could be a redshift effect, since more high-stretch, bright SNeIa are found at high redshift (Smith et al. 2012). Furthermore, LOSS was not a blind survey, meaning that host galaxy selection could affect the luminosity distribution. Regardless of these potential explanations, the LOSS sample is too small to conclude whether the dimmer magnitudes are a statistical fluctuation or not.

The limited available data sets also pose the most important restriction on the accuracy of the color and stretch distributions, as the amount of data used for the analysis of K13 only allowed for a rough fit of the simulated distributions of x_1 and c to those observed in SDSS and SNLS. With larger future data sets, a population model should be constructed from fitting functions with large numbers of degrees of freedom, including a dependence on redshift and host galaxy properties.

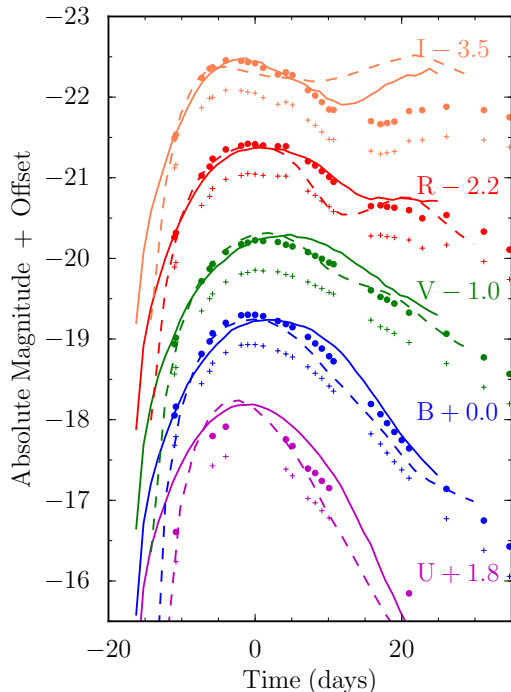


Figure 13. Visual light curve comparison. The dots and crosses show the light curves of 2003du (Stanishev et al. 2007) for the two different distance moduli suggested in their paper, 32.79 (dots) and 32.42 (crosses). The solid lines show light curves of the 88° viewing angle of the KRW09_iso_6_dc_2 model. The dashed lines show light curves of the W7 model.

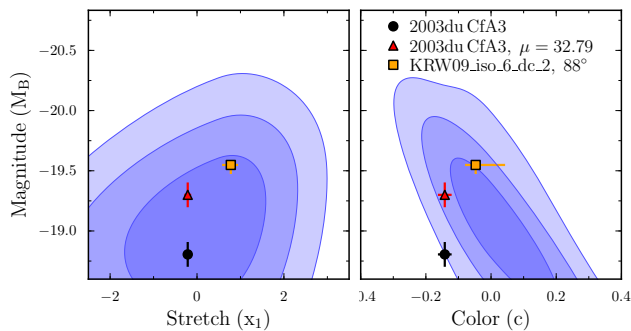


Figure 14. Fit results for the KRW09_iso_6_dc_2 delayed-detonation model (orange square) and the observed SN 2003du (CfA3 data, black circle). If we assume the absolute magnitude resulting from the data of Stanishev et al. (2007) and their suggested distance modulus of $\mu = 32.79$, the point shifts to $M_B = -19.3$ (red triangle). While the fitted parameters of both KRW09_iso_6_dc_2 and 2003du are in good agreement with observations, they occupy different loci on the parameter planes, depending on which distance modulus is assumed. Furthermore, the assumed distance modulus determines whether 2003du is a “normal” SN in the sense that it lies close to the center of the color–magnitude distribution. See Section 4.2 for a detailed discussion.

Such an investigation is beyond the scope of this paper, but is a promising avenue for future research, particularly once DES data will be available.

4.2. The Perils of Visual Light Curve Comparisons

We have previously alluded to issues with visual comparisons between simulated and observed light curves. In some cases, only a rough comparison with light curves is desired, for example if an explosion model is not intended to represent normal SNeIa but a sub-group such as sub-luminous events. In such cases, visual comparisons are perfectly ap-

propriate (e.g. Kromer et al. 2013). Often, however, the purpose of visual comparisons is to determine whether an explosion model reproduces the light curves of normal SNeIa (see, e.g., Woosley et al. 2007; Kromer et al. 2010; Jack et al. 2011; Pakmor et al. 2012). Here we investigate a particular example of this technique. Both KRW09 and Blondin et al. (2011) overplot light curves of the KRW09_iso_6_dc_2 model (88° viewing angle) and the observed SNIa 2003du, and note that there is good visual agreement. In general, our analysis agrees, since the particular viewing angle receives a figure of merit for goodness-of-fit of $\langle f_{\chi^2} \rangle = 0.83$. However, on closer inspection of the light curve fit (third column of Figure 7), we note that the fit is $\approx 1.6\sigma$ off the best-fit SALT2 model on average, and shows somewhat poor agreement at early times. In this section, we investigate the reasons why those discrepancies are not apparent in the visual comparison of light curves. We emphasize that we pick the example of KRW09_iso_6_dc_2 because the explosion model light curves have already been analyzed in this paper, not because it represents a particularly good or bad choice of data to compare to.

First, and most importantly, the distance modulus to 2003du, and thus its magnitude, are highly uncertain. Stanishev et al. (2007) quote two different distance moduli of $\mu = 32.42$ and $\mu = 32.79$, leading to a 0.37 magnitude difference. The reason for this uncertainty is the uncertain peculiar velocity of the host galaxy of 2003du which could be a few hundred km s^{-1} , corresponding to a redshift uncertainty $\sigma_z \approx 0.001$. Given that the redshift of 2003du is $z = 0.007$, this uncertainty leads to a 0.3 magnitude uncertainty. Clearly, using very nearby SNe for absolute magnitude comparisons is dangerous. Using $\mu = 32.79$, the value adopted in Kasen et al. (2009), 2003du has $M_B = -19.30$ (Stanishev et al. 2007), a value which coincides well with the KRW09_iso_6_dc_2 model. Figure 13 shows a visual comparison of the *UBVRI* light curves of 2003du and the 88° viewing angle of the KRW09_iso_6_dc_2 model. For comparison, the 2003du light curves are also plotted using the alternative distance modulus of $\mu = 32.42$ which leads to a catastrophic fit.

Secondly, the light curve fit to the 88° viewing angle of KRW09_iso_6_dc_2 is not as good as the visual comparison suggests, particularly at early epochs (Figure 7). Returning to the visual comparison shown in Figure 13, we notice that the rising slope of KRW09_iso_6_dc_2 is indeed quite shallow compared to the W7 model (dashed lines). The shallow rising slope of some of the KRW09 models was pointed out in Figure 8 of Blondin et al. (2011), but the comparison to 2003du does not highlight this issue, since there are few data points at early times. Our fitting method captures the different rising slopes by assigning the KRW09_iso_6_dc_2 model a larger stretch than 2003du (Figure 14).

Finally, we need to address the question whether 2003du is a truly “photometrically normal” SNIa as claimed by Stanishev et al. (2007). Figure 14 shows the fitted parameters for 2003du, using CfA3 observations. Given the redshift assumed in the survey data, the fitted absolute magnitude of 2003du is -18.81 . With this magnitude, 2003du lies at the center of the stretch–magnitude distribution, but somewhat off the main color–magnitude relation and has a figure of merit of $f_{\chi^2} = 0.60$ (black circle). If we use the peak magnitude derived from the larger distance modulus, $M_B = -19.3$, 2003du moves toward the center of the color–magnitude relation and receives $f_{\chi^2} = 0.79$ (red triangle). Either way 2003du is lo-

cated at the blue end of the bulk distribution, and while it may qualify as a “photometrically normal” SNIa, it is not an ideal candidate for light curve comparisons.

In summary, there are good reasons to be careful with visual light curve comparisons, most importantly that features such as a shallow rising slope can easily be missed. 2003du is a particularly unfortunate case where a large uncertainty in the distance modulus makes any inference about explosion models difficult.

5. CONCLUSION

We have presented a new method to evaluate explosion model light curves using observed data. We rely on a data-driven model to represent the heterogeneous family of SNIa light curves. For this purpose, we choose the most recently trained model, SALT2. For each explosion model, we perform multiple fits to the SALT2 model using a wide range of reasonable choices for filter bands and epoch range, since those choices affect the fit results. For each fit, we derive fit results in the SALT2 parameter space of stretch, color and magnitude. We take the weighted mean of those parameters to be the best estimate of the fit results for a given set of explosion model light curves. We compare the fitted parameters to a parametric population model in stretch–color–magnitude space which we construct from the color and stretch distributions of K13, and values for α , β , and M_0 from the literature. We extend this population model with small outlier populations in color and magnitude to account for observed outlier events in a nearby data set. The final figure of merit is composed of two individual figures of merit for the goodness-of-fit of a light curve, and for the likelihood of observing an event with the fitted stretch, color and magnitude in nature.

We have used this method to evaluate a variety of explosion models, and found their figures of merit to range from 0.124 to 0.909, given an allowed range of 0 (worst) to 1 (best). We found the delayed-detonation models of KRW09 to agree well with observed light curves, particularly the isotropic models. We confirmed that the W7 model also matches observed light curves well. We found a wide range of figures of merit for the pure-deflagration models analyzed, clearly distinguishing between the few-bubble and many-bubble variations of those models. Finally, we found that a suite of off-centered detonation models does not reproduce the stretch–magnitude and color–magnitude relations.

We discussed uncertainties on our population model, and concluded that our model is remarkably stable within the current uncertainties on the SALT2 parameters α and β . However, due to the uncertainty in H_0 it is still somewhat difficult to define the absolute magnitudes of SNIa to the desired accuracy. We conclude that our population model is valid within the latest cosmological limits on H_0 , but that future measurements might shift the overall magnitude distribution. Furthermore, we investigated some seemingly contradictory inferences from visual light curve comparisons and our method. We concluded that visual light curve comparisons can be misleading, particularly if the absolute magnitude of the observed SNIa is not well determined.

We have left various promising avenues of research for future investigations, and briefly discuss a few of them. First, we did not consider the IR regions of the explosion model light curves since they are notoriously difficult to model accurately in radiative transfer calculations. Our method could easily be extended by using a data-driven model which covers the IR, such as SNooPy. Using a different data-driven model, how-

ever, would mean having to develop a new population model in the new parameter space.

Secondly, our analysis neglected the time of explosion which is known for explosion models. While the time between explosion and peak brightness is unknown for individual observed SNIa, recent observations have shown the slope of the rising light curves to closely follow a t^2 law. This behavior was demonstrated for observations of a single well-observed SNIa (Nugent et al. 2011), the statistical average of a large sample (Hayden et al. 2010; Ganeshalingam et al. 2011) and through analytical modeling (Piro & Nakar 2012, and references therein). The t^2 dependence could be used to extrapolate the SALT2 model to very early times, and thus include the time of explosion as a data point in the light curve fit. The constraint of zero flux at explosion would place tight constraints on the rising light curves produced by explosion models, which have been found to be too shallow in various explosion models.

Third, there are uncertainties in our population model which are difficult to address with current data, such as the best functional form to parameterize the distributions of stretch and color, the tails of these distributions at extreme, rare values, as well as the dependence of the population model on redshift. Given the larger data sets of the future, we envision a global fit of the data to a function with many free parameters. As with the analysis of K13, such strategies still have to rely on an accurate model of survey biases.

Finally, data-driven models do not parameterize peculiar SNIa. Thus, our method assigns explosion models with peculiar light curves a relatively low figure of merit, even though they might match peculiar SNIa observed in nature. For explosion models which might reproduce peculiar SNIa such as sub-luminous Type Iax, we could use the photometric classification algorithm of Sako et al. (2011). In this analysis, core-collapse SN templates are replaced with templates for peculiar SNIa, and explosion models are identified as either a normal SNIa or any of the known peculiar-Ia. Such a method could also be applied to the light curves of double-degenerate explosion models to investigate whether they resemble normal Type Ia, or peculiar objects.

ACKNOWLEDGMENTS

We thank Dan Kasen for providing the SEDs of the KRW09 explosion models. We are grateful to Sean Couch and Emille Ishida for a careful reading of the draft and their comments. We are indebted to Tom Loredo for fruitful discussions about the statistical aspects of our method, and to Mark Sullivan for his comments on extinction. R.K. is grateful for the support of National Science Foundation grant 1009457, and of the Kavli Institute for Cosmological Physics. This work was supported in part by the University of Chicago and the Department of Energy under section H44 of Department of Energy Contract No. DE-AC02-07CH11359 awarded to Fermi Research Alliance LLC, and by the National Science Foundation under grant AST-0909132, as well as NASA award NNX09AK60G.

REFERENCES

- Aldering, G., et al. 2006, ApJ, 650, 510
- Astier, P., et al. 2006, A&A, 447, 31
- Baron, E., Bongard, S., Branch, D., & Hauschildt, P. H. 2006, ApJ, 645, 480
- Benetti, S., et al. 2005, ApJ, 623, 1011
- Bernstein, J. P., et al. 2012, ApJ, 753, 152
- Bessell, M. S. 1990, PASP, 102, 1181
- Blondin, S., Dessart, L., Hillier, D. J., & Khokhlov, A. M. 2013, MNRAS, 429, 2127

- Blondin, S., Kasen, D., Röpke, F. K., Kirshner, R. P., & Mandel, K. S. 2011, *MNRAS*, 417, 1280
- Blondin, S., & Tonry, J. L. 2011, in *Astrophysics Source Code Library*, record ascl:1107.001, 7001
- Blondin, S., et al. 2012, *AJ*, 143, 126
- Branch, D., et al. 2006, *PASP*, 118, 560
- Brown, P. J., et al. 2012, *ApJ*, 753, 22
- Burns, C. R., et al. 2011, *AJ*, 141, 19
- Campbell, H., et al. 2013, *ApJ*, 763, 88
- Chornock, R., Filippenko, A. V., Branch, D., Foley, R. J., Jha, S., & Li, W. 2006, *PASP*, 118, 722
- Conley, A., et al. 2008, *ApJ*, 681, 482
- , 2011, *ApJS*, 192, 1
- Dan, M., Rosswog, S., Guillochon, J., & Ramirez-Ruiz, E. 2011, *ApJ*, 737, 89
- , 2012, *MNRAS*, 422, 2417
- Filippenko, A. V., Li, W. D., Treffers, R. R., & Modjaz, M. 2001, in *Astronomical Society of the Pacific Conference Series*, Vol. 246, IAU Colloq. 183: Small Telescope Astronomy on Global Scales, ed. B. Paczynski, W.-P. Chen, & C. Lemme, 121
- Folatelli, G., et al. 2010, *AJ*, 139, 120
- Foley, R. J., et al. 2013, *ApJ*, 767, 57
- Frieman, J. A., et al. 2008, *AJ*, 135, 338
- Fryxell, B., et al. 2000, *ApJS*, 131, 273
- Fukugita, M., Ichikawa, T., Gunn, J. E., Doi, M., Shimasaku, K., & Schneider, D. P. 1996, *AJ*, 111, 1748
- Ganeshalingam, M., Li, W., & Filippenko, A. V. 2011, *MNRAS*, 416, 2607
- Goobar, A., & Leibundgut, B. 2011, *Annual Review of Nuclear and Particle Science*, 61, 251
- Gunn, J. E., et al. 1998, *AJ*, 116, 3040
- , 2006, *AJ*, 131, 2332
- Guy, J., Astier, P., Nobili, S., Regnault, N., & Pain, R. 2005, *A&A*, 443, 781
- Guy, J., et al. 2007, *A&A*, 466, 11
- , 2010, *A&A*, 523, A7+
- Hatano, K., Branch, D., & Deaton, J. 1998, *ApJ*, 502, 177
- Hauschildt, P. H., & Baron, E. 1999, *Journal of Computational and Applied Mathematics*, 109, 41
- , 2004, *A&A*, 417, 317
- Hayden, B. T., et al. 2010, *ApJ*, 712, 350
- Hicken, M., Wood-Vasey, W. M., Blondin, S., Challis, P., Jha, S., Kelly, P. L., Rest, A., & Kirshner, R. P. 2009, *ApJ*, 700, 1097
- Hillebrandt, W., Kromer, M., Röpke, F. K., & Ruiter, A. J. 2013, *Frontiers of Physics*, 8, 116
- Hillebrandt, W., & Niemeyer, J. C. 2000, *ARA&A*, 38, 191
- Hinshaw, G., et al. 2012, arXiv:1212.5226
- Höflich, P. 1995, *ApJ*, 443, 89
- Höflich, P., & Khokhlov, A. 1996, *ApJ*, 457, 500
- Höflich, P., Khokhlov, A., Wheeler, J. C., Phillips, M. M., Suntzeff, N. B., & Hamuy, M. 1996, *ApJ*, 472, L81
- Höflich, P., et al. 2010, *ApJ*, 710, 444
- Holtzman, J. A., et al. 2008, *AJ*, 136, 2306
- Hsiao, E. Y., Conley, A., Howell, D. A., Sullivan, M., Pritchett, C. J., Carlberg, R. G., Nugent, P. E., & Phillips, M. M. 2007, *ApJ*, 663, 1187
- Iben, Jr., I., & Tutukov, A. V. 1984, *ApJS*, 54, 335
- Ivezic, Z., et al. 2008, arXiv:0805.2366
- Jack, D., Hauschildt, P. H., & Baron, E. 2011, *A&A*, 528, A141
- Jeffery, D. J., Leibundgut, B., Kirshner, R. P., Benetti, S., Branch, D., & Sonneborn, G. 1992, *ApJ*, 397, 304
- Jha, S., Riess, A. G., & Kirshner, R. P. 2007, *ApJ*, 659, 122
- Jordan, IV, G. C., Fisher, R. T., Townsley, D. M., Calder, A. C., Graziani, C., Asida, S., Lamb, D. Q., & Truran, J. W. 2008, *ApJ*, 681, 1448
- Jordan, IV, G. C., Perets, H. B., Fisher, R. T., & van Rossum, D. R. 2012a, *ApJ*, 761, L23
- Jordan, IV, G. C., et al. 2012b, *ApJ*, 759, 53
- Kasen, D. 2006, *ApJ*, 649, 939
- Kasen, D., & Plewa, T. 2007, *ApJ*, 662, 459
- Kasen, D., Röpke, F. K., & Woosley, S. E. 2009, *Nature*, 460, 869
- Kasen, D., Thomas, R. C., & Nugent, P. 2006, *ApJ*, 651, 366
- Kasen, D., & Woosley, S. E. 2007, *ApJ*, 656, 661
- Kelly, P. L., Hicken, M., Burke, D. L., Mandel, K. S., & Kirshner, R. P. 2010, *ApJ*, 715, 743
- Kessler, R., et al. 2009, *PASP*, 121, 1028
- , 2013, *ApJ*, 764, 48
- Khokhlov, A., Mueller, E., & Höflich, P. 1993, *A&A*, 270, 223
- Khokhlov, A. M. 1991, *A&A*, 245, 114
- Kromer, M., & Sim, S. A. 2009, *MNRAS*, 398, 1809
- Kromer, M., Sim, S. A., Fink, M., Röpke, F. K., Seitzzahl, I. R., & Hillebrandt, W. 2010, *ApJ*, 719, 1067
- Kromer, M., et al. 2013, *MNRAS*, 429, 2287
- Krueger, B. K., Jackson, A. P., Calder, A. C., Townsley, D. M., Brown, E. F., & Timmes, F. X. 2012, *ApJ*, 757, 175
- Lampeitl, H., et al. 2010, *ApJ*, 722, 566
- Leaman, J., Li, W., Chornock, R., & Filippenko, A. V. 2011, *MNRAS*, 412, 1419
- Li, W., et al. 2003, *PASP*, 115, 453
- , 2011a, *Nature*, 480, 348
- , 2011b, *MNRAS*, 412, 1441
- Livne, E., & Arnett, D. 1995, *ApJ*, 452, 62
- Maeda, K., et al. 2011, *MNRAS*, 413, 3075
- Maoz, D., & Mannucci, F. 2012, *Publications of the Astronomical Society of Australia*, 29, 447
- Marriner, J., et al. 2011, *ApJ*, 740, 72
- Meakin, C. A., Seitzzahl, I., Townsley, D., Jordan, G. C., Truran, J., & Lamb, D. 2009, *ApJ*, 693, 1188
- Niemeyer, J. C. 1999, *ApJ*, 523, L57
- Niemeyer, J. C., & Hillebrandt, W. 1995, *ApJ*, 452, 769
- Niemeyer, J. C., & Woosley, S. E. 1997, *ApJ*, 475, 740
- Nomoto, K., Thielemann, F.-K., & Yokoi, K. 1984, *ApJ*, 286, 644
- Nugent, P., Baron, E., Branch, D., Fisher, A., & Hauschildt, P. H. 1997, *ApJ*, 485, 812
- Nugent, P., Kim, A., & Perlmutter, S. 2002, *PASP*, 114, 803
- Nugent, P. E., et al. 2011, *Nature*, 480, 344
- Pakmor, R., Kromer, M., Taubenberger, S., Sim, S. A., Röpke, F. K., & Hillebrandt, W. 2012, *ApJ*, 747, L10
- Perlmutter, S., et al. 1999, *ApJ*, 517, 565
- Phillips, M. M. 1993, *ApJ*, 413, L105
- Phillips, M. M., Lira, P., Suntzeff, N. B., Schommer, R. A., Hamuy, M., & Maza, J. 1999, *AJ*, 118, 1766
- Phillips, M. M., et al. 2007, *PASP*, 119, 360
- Piro, A. L., & Nakar, E. 2012, arXiv:1211.6438
- Planck Collaboration et al. 2013, arXiv:1303.5076
- Plewa, T., Calder, A. C., & Lamb, D. Q. 2004, *ApJ*, 612, L37
- Prieto, J. L., et al. 2007, arXiv:0706.4088
- Riello, M., & Patat, F. 2005, *MNRAS*, 362, 671
- Riess, A. G., Press, W. H., & Kirshner, R. P. 1996a, *ApJ*, 473, 88
- , 1996b, *ApJ*, 473, 588
- Riess, A. G., et al. 1998, *AJ*, 116, 1009
- , 2011, *ApJ*, 730, 119
- Röpke, F. K. 2007, *ApJ*, 668, 1103
- Röpke, F. K., & Niemeyer, J. C. 2007, *A&A*, 464, 683
- Röpke, F. K., et al. 2012, *ApJ*, 750, L19
- Sako, M., et al. 2008, *AJ*, 135, 348
- , 2011, *ApJ*, 738, 162
- Seitzzahl, I. R., et al. 2013, *MNRAS*, 429, 1156
- Shen, K. J., Kasen, D., Weinberg, N. N., Bildsten, L., & Scannapieco, E. 2010, *ApJ*, 715, 767
- Silverman, J. M., Ganeshalingam, M., Li, W., & Filippenko, A. V. 2012, *MNRAS*, 425, 1889
- Smith, M., et al. 2012, *ApJ*, 755, 61
- Stanishev, V., et al. 2007, *A&A*, 469, 645
- Sullivan, M., et al. 2006, *ApJ*, 648, 868
- , 2010, *MNRAS*, 406, 782
- , 2011, *ApJ*, 737, 102
- Thielemann, F.-K., Nomoto, K., & Yokoi, K. 1986, *A&A*, 158, 17
- Tonry, J. L., et al. 2012, *ApJ*, 750, 99
- Townsley, D. M., Calder, A. C., Asida, S. M., Seitzzahl, I. R., Peng, F., Vladimirova, N., Lamb, D. Q., & Truran, J. W. 2007, *ApJ*, 668, 1118
- Tripp, R. 1998, *A&A*, 331, 815
- van Rossum, D. R. 2012, *ApJ*, 756, 31
- Wang, L., Goldhaber, G., Aldering, G., & Perlmutter, S. 2003, *ApJ*, 590, 944
- Whelan, J., & Iben, Jr., I. 1973, *ApJ*, 186, 1007
- Wood-Vasey, W. M., Aldering, G., Nugent, P., Helin, E. F., Pravdo, S., Hicks, M., & Lawrence, K. 2002, *IAU Circ.*, 7902, 3
- Wood-Vasey, W. M., et al. 2007, *ApJ*, 666, 694
- Woosley, S. E. 2007, *ApJ*, 668, 1109
- Woosley, S. E., Kasen, D., Blinnikov, S., & Sorokina, E. 2007, *ApJ*, 662, 487
- Woosley, S. E., Kerstein, A. R., Sankaran, V., Aspden, A. J., & Röpke, F. K. 2009, *ApJ*, 704, 255
- Yasuda, N., & Fukugita, M. 2010, *AJ*, 139, 39
- York, D. G., et al. 2000, *AJ*, 120, 1579

APPENDIX

A. SURVEY DATA

Here we briefly review the survey data which were used to check the consistency of our population model in Section 2.4, and to extend it to represent outliers in color and magnitude. We describe the SDSS and CfA3 surveys, the selection cuts applied to these samples, and our procedure to reconstruct the rest-frame peak magnitude. We note that the population model of K13 itself

was based on both the SDSS and SNLS (G10) surveys, and refer the reader to those papers for detailed information on the data sets.

A.1. The SDSS Survey

The SDSS-II Supernova Survey (York et al. 2000; Frieman et al. 2008) used the SDSS camera and telescope (Gunn et al. 1998, 2006) to search for SNe in three seasons from 2005 to 2007 (Sako et al. 2008). The survey scanned a 300 deg² region called Stripe 82 with a typical cadence of four nights, obtaining images in the *ugriz* filter bands (Fukugita et al. 1996). The final SNIa photometry was derived using the Scene Modeling Photometry technique (Holtzman et al. 2008), and used in this paper as well as K13. The SDSS survey discovered about 500 spectroscopically confirmed SNeIa.

A.2. The CfA3 Survey

The CfA3 survey (Hicken et al. 2009) was conducted between 2001 and 2008 at the F. L. Whipple Observatory of the Harvard-Smithsonian Center for Astrophysics (CfA). The survey recorded a total of 11,500 observations of 185 SNeIa below $z = 0.08$. Over its lifetime, CfA3 used two cameras, 4Shooter and Keplercam. The Johnson *U*, *B* and *V* filters were used on all three cameras, but the IR filters were changed during the survey. Unlike SDSS, the CfA3 survey did not discover SNeIa itself, but followed up discoveries by other groups and amateur astronomers, about half of them from the LOSS (Filippenko et al. 2001). Hicken et al. (2009) emphasize that the CfA3 sample is not representative of the underlying SNIa population since the observing strategy favored young and extreme events.

A.3. Selection Cuts

The SDSS and CfA3 samples used in Section 2.4 were fit with SALT2 using SNANA. In order to ensure reliable light curve fits, we applied the following selection cuts:

- At least three filters need to have at least one observation each with signal-to-noise ratio > 5 .
- There must be at least one observation before *B*-band peak, and at least one later than 10 rest-frame days after peak. This criterion ensures that x_1 is somewhat constrained.
- There must be a total of at least 12 observations in all filters combined.
- The fit probability (as derived from χ^2/N_{dof}) is at least 1%.
- The SN must be a confirmed Type Ia event.

These cuts are deliberately not too strict, since we do not want to exclude interesting populations which might deviate from our population model.

A.4. Reconstruction of Rest-frame Magnitudes

A SALT2 fit to observed SNeIa returns values for m_B , the peak magnitude in a *redshifted B*-band, for $x_1 = c = 0$. For the purpose of comparing explosion models to data, however, we are interested in the *rest-frame* characteristics of an explosion, namely the best-fit, rest-frame, *B*-band peak magnitude, M_B^{rest} . As we generate our mock light curves of the explosion models at a negligible redshift, $M_B^{\text{rest}} \approx m_B - \mu$. For observed SNeIa at higher redshift, however, the filter transmission function for *B*-band is redshifted between the rest and observer frames, meaning that K-corrections are necessary to translate between m_B and M_B^{rest} . For observed SNeIa at higher redshift, appropriate K-corrections are used to compute M_B^{rest} .

B. POPULATION MODEL

In Section 2.4 we stated the probability distribution for our population model. Here, we derive it more rigorously, and compute marginalized probability distributions in two variables. We assume that the variables $\mathbf{x} = (x_1, c, \Delta_M)$ are independent and Gaussian. For now, we ignore their asymmetric σ values and their potentially non-zero means. We can write the probability density as a trivariate Gaussian, $dP(x_1, c, \Delta_M) = N e^{\frac{1}{2}\mathbf{x}^T C^{-1} \mathbf{x}} dx_1 dc d\Delta_M$ with $C^{-1} = \text{diag}(\sigma_{x_1}^{-2}, \sigma_c^{-2}, \sigma_M^{-2})$. The transformation to the desired parameter space $\mathbf{y} = (x_1, c, M_B)$ is given by $\mathbf{y} = T\mathbf{x}$, where T and the new inverse covariance matrix D^{-1} are

$$T = \begin{pmatrix} 1 & 0 & 0 \\ 0 & 1 & 0 \\ -\alpha & \beta & 1 \end{pmatrix} \implies D^{-1} = (T^{-1})^T C^{-1} (T^{-1}) = \begin{pmatrix} \sigma_{x_1}^{-2} + \alpha^2 \sigma_M^{-2} & -\alpha\beta\sigma_M^{-2} & \alpha\sigma_M^{-2} \\ -\alpha\beta\sigma_M^{-2} & \sigma_c^{-2} + \beta^2\sigma_M^{-2} & -\beta^2\sigma_M^{-2} \\ \alpha\sigma_M^{-2} & -\beta^2\sigma_M^{-2} & \sigma_M^{-2} \end{pmatrix}. \quad (\text{B1})$$

The probability density is now

$$dP(x_1, c, M_B) = N \exp\left[\frac{1}{2}\mathbf{y}^T D^{-1} \mathbf{y}\right] dx_1 dc dM_B = N \exp\left[\frac{x_1^2}{\sigma_{x_1}^2} + \frac{c^2}{\sigma_c^2} + \frac{(M_B + \alpha x_1 - \beta c)^2}{\sigma_M^2}\right] dx_1 dc dM_B. \quad (\text{B2})$$

Inserting the mean values μ_{x_1} , μ_c and μ_M recovers Equation (9). As explained in Section 2.4, one Gaussian probability function per parameter does not capture outliers in color and magnitude. Thus, we represent each parameter by a sum of Gaussians with

independent means, lower and upper variances such that

$$\frac{dP(\theta)}{d\theta} = \sum_i \sqrt{\frac{2}{\pi}} \frac{w_i}{(\sigma_{\theta+,i} + \sigma_{\theta-,i})} \begin{cases} \exp\left(\frac{(\theta - \mu_{\theta,i})^2}{2\sigma_{\theta+,i}^2}\right) & \forall \theta > \mu_{\theta,i} \\ \exp\left(\frac{(\theta - \mu_{\theta,i})^2}{2\sigma_{\theta-,i}^2}\right) & \forall \theta < \mu_{\theta,i} \end{cases} \quad (\text{B3})$$

where the weights w_i sum to 1. Due to the linearity of the system, all the above equations still hold for the sums of Gaussians. The remaining challenge is to marginalize the distribution over each one of the variables to obtain probability contours in planes of two variables for plotting. For any combination of x_1 , c and the corrected magnitude, $M_B + \alpha x_1 - \beta c$, their probability distributions are linear sums of independent Gaussians (Figure 5). In the cases of the $x_1 - M_B$ and $c - M_B$ planes, however, we need to integrate over the asymmetric Gaussian distributions of both the third variable and M_B (since it is not independent of the third variable). For the case of integrating over i Gaussians in x_1 , their \pm asymmetry, and j (symmetric) Gaussians in M_B , we obtain

$$\begin{aligned} \frac{dP(c, M_B)}{dc dM_B} &= \frac{dP(c)}{dc} \sum_i \sum_j \sum_{\pm} \sqrt{\frac{2}{\pi}} \frac{w_{x1,i}}{(\sigma_{x1+,i} + \sigma_{x1-,i})} \frac{w_{M,j}}{2\sigma_{M,j}} \left(\frac{1}{\sigma_{x1,i\pm}^2} + \frac{\alpha^2}{\sigma_{M,j}^2} \right)^{-\frac{1}{2}} \\ &\times \exp\left[\frac{(M_B - \mu_{M,j} + \alpha\mu_{x1,i} - \beta c)^2}{(\sigma_{M,j}^2 + \alpha^2\sigma_{x1,i\pm}^2)} \right] \times \left[1 \pm \operatorname{erf}\left(\frac{\alpha\sigma_{x1,i\pm} (M_B - \mu_{M,j} + \alpha\mu_{x1,i} - \beta c)}{\sqrt{2}\sigma_{M,j} \sqrt{\sigma_{M,j}^2 + \alpha^2\sigma_{x1,i\pm}^2}} \right) \right] \end{aligned} \quad (\text{B4})$$

and similarly

$$\begin{aligned} \frac{dP(x_1, M_B)}{dx_1 dM_B} &= \frac{dP(x_1)}{dx_1} \sum_i \sum_j \sum_{\pm} \sqrt{\frac{2}{\pi}} \frac{w_{c,i}}{(\sigma_{c+,i} + \sigma_{c-,i})} \frac{w_{M,j}}{2\sigma_{M,j}} \left(\frac{1}{\sigma_{c,i\pm}^2} + \frac{\beta^2}{\sigma_{M,j}^2} \right)^{-\frac{1}{2}} \\ &\times \exp\left[\frac{(M_B - \mu_{M,j} + \alpha x_1 - \beta\mu_{c,i})^2}{(\sigma_{M,j}^2 + \beta^2\sigma_{c,i\pm}^2)} \right] \times \left[1 \mp \operatorname{erf}\left(\frac{\beta\sigma_{c,i\pm} (M_B - \mu_{M,j} + \alpha x_1 - \beta\mu_{c,i})}{\sqrt{2}\sigma_{M,j} \sqrt{\sigma_{M,j}^2 + \beta^2\sigma_{c,i\pm}^2}} \right) \right]. \end{aligned} \quad (\text{B5})$$

The confidence contours for these probability distributions were computed numerically, and are shown in Figure 4(c).